Infrared Photodetectors based on Nanowire Arrays with Embedded Quantum Heterostructures

Karimi, Mohammad

2020

Document Version:
Publisher's PDF, also known as Version of record

Link to publication

Citation for published version (APA):
Karimi, M. (2020). *Infrared Photodetectors based on Nanowire Arrays with Embedded Quantum Heterostructures*. Department of Physics, Lund University.

Total number of authors:
1

LUND UNIVERSITY

PO Box 117
221 00 Lund
+46 46-222 00 00

Infrared Photodetectors based on Nanowire Arrays with Embedded Quantum Heterostructures

MOHAMMAD KARIMI
DEPARTMENT OF PHYSICS | FACULTY OF ENGINEERING | LUND UNIVERSITY

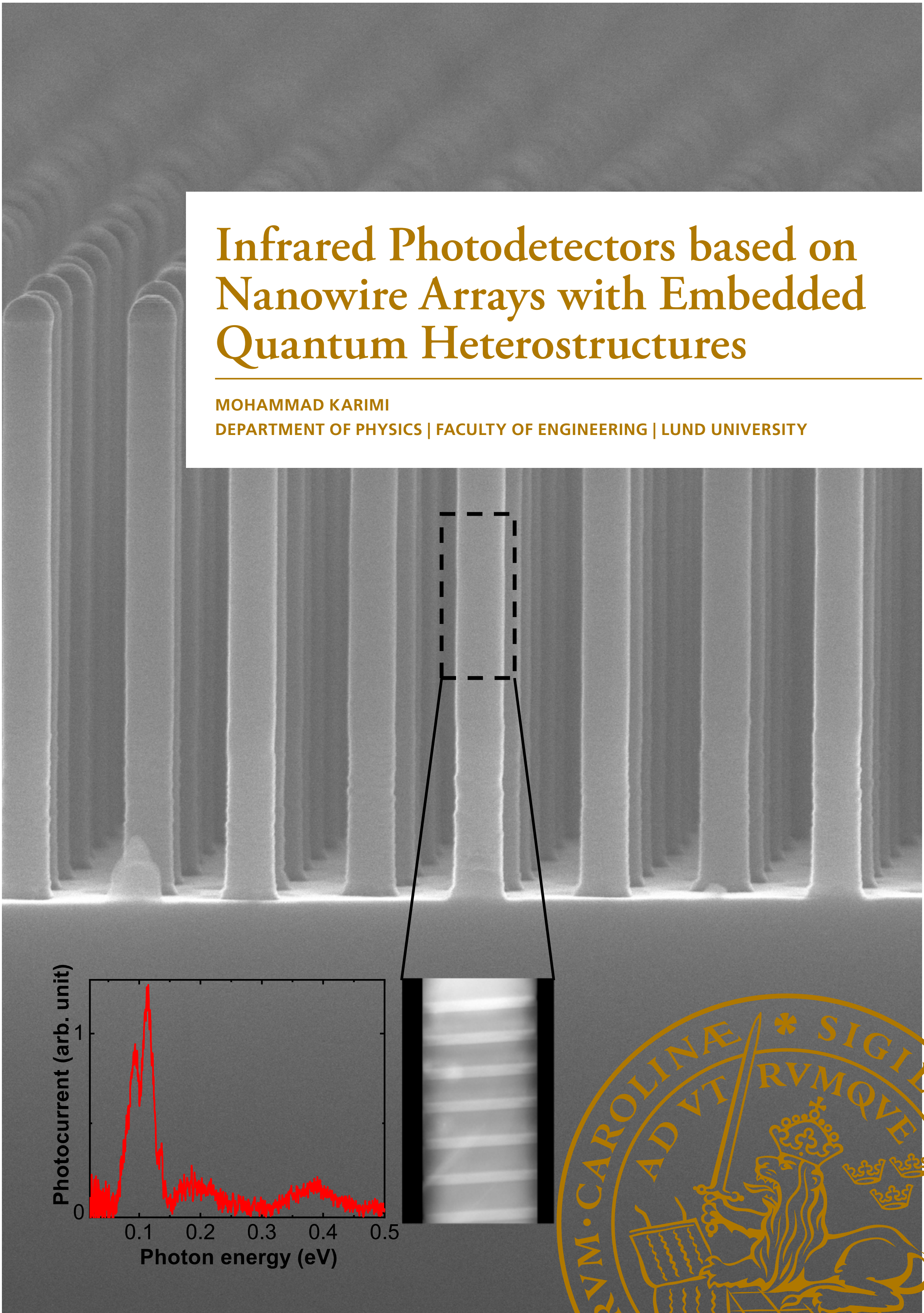

Infrared Photodetectors based on Nanowire Arrays with Embedded Quantum Heterostructures

Infrared Photodetectors based on Nanowire Arrays with Embedded Quantum Heterostructures

Mohammad Karimi

Division of Solid State Physics
Department of Physics
Lund University

DOCTORAL DISSERTATION
by due permission of the Faculty of Engineering, Lund University, Sweden.
To be publicly defended on Friday, February 28th, 2020 at 13.15 in Rydbergsalen,
for the degree of Doctor of Philosophy in Engineering.

Faculty opponent
Professor Manijeh Razeghi
Northwestern University, USA

Organization LUND UNIVERSITY Division of Solid State Physics Department of Physics, Lund, Sweden	**Document name**: Doctoral Dissertation **Date of issue:** 2020-02-28 **Author:** Mohammad Karimi

Title: Infrared Photodetectors based on Nanowire Arrays with Embedded Quantum Heterostructures

Abstract

Optical sensors operating in the infrared range of the electromagnetic spectrum are key components in a variety of applications including optical communication, night vision, medical diagnosis, surveillance, and astronomy. Semiconductor nanowires have great potential for realizing broadband infrared photodetectors with excellent responsivity, low dark current and low noise, and a unique compatibility with commercial silicon-based electronics. In this thesis work, comprising three published articles in Nano Letters, we synthesized, characterized and modeled disruptive infrared photodetectors based on InP nanowires with axially embedded InAsP quantum discs.

In the first article, we made a combined study of design, growth, device processing and optoelectronic properties of n^+−i−n^+ InP detector elements comprising 4 million periodically ordered nanowires in arrays, including either a single or 20 InAsP quantum discs. Optimized Zn compensation of the residual non-intentional n-dopants in the i-segment suppressed the dark current at room-temperature to a few pA/NW. The detector elements exhibit a strong broadband photoresponse with contributions from both the InP and InAsP segments with a threshold wavelength of about 2.0 μm and a bias-tunable responsivity reaching 7 A/W@ 1.38 μm at 2 V bias.

In the second article, we performed an in-depth experimental and theoretical investigation of the responsivity of optimized photodetectors under different illumination conditions. The photodetectors exhibit strongly bias and power-dependent responsivities reaching record-high values of 250 A/W at 980 nm/20 nW and 990 A/W at 532 nm/60 nW, both at 3.5 V bias. Complementary real device modeling revealed a new photogating mechanism, induced by the complex charge carrier dynamics involving optical excitation and recombination in the quantum discs and interface traps, which reduces the electron transport barrier between the n^+ segment and the i-segment under illumination.

Finally, in the last article, we demonstrate the first intersubband photocurrent response in a nanowire heterostructure array photodetector. The infrared response from 3 to 20 μm is enabled by intersubband transitions in the low-bandgap InAsP quantum discs. The intriguing optical characteristics, including unexpected sensitivity to normal incident radiation, are partly explained by excitation of the longitudinal component of optical modes in the photonic crystal formed by the nanostructured portion of the detectors.

Our results show that properly designed arrays of axial nanowire heterostructures are promising candidates for realization of commercially viable broadband photodetectors.

Key words: Nanowires, infrared photodetectors, quantum discs-in-nanowire, nanowire array, high responsivity, intersubband nanowire photodetector

Classification system and/or index terms (if any)		
Supplementary bibliographical information		Language: English
ISSN and key title		ISBN 978-91-7895-414-8 (Print) ISBN 978-91-7895-415-5 (Electronic)
Recipient's notes	Number of pages: 78	Price
	Security classification	

I, the undersigned, being the copyright owner of the abstract of the above-mentioned dissertation, hereby grant to all reference sources permission to publish and disseminate the abstract of the above-mentioned dissertation.

Signature Mohammad Karimi Date 2020-01-20

Infrared Photodetectors based on Nanowire Arrays with Embedded Quantum Heterostructures

Mohammad Karimi

Faculty of Engineering
Department of Physics
Solid State Physics
Lund University
P.O.Box 118
SE-221 00 Lund
Sweden

ISBN 978-91-7895-414-8 (Print)
ISBN 978-91-7895-415-5 (Electronic)

Printed in Sweden by Media-Tryck, Lund University
Lund 2020

Printed matter
3041 0903

Media-Tryck is a Nordic Swan Ecolabel
certified provider of printed material.
Read more about our environmental
work at www.mediatryck.lu.se

MADE IN SWEDEN

In dedication to all whom I love dearly

Physics isn't the most important thing. Love is.

–Richard P. Feynman

No, this trick won't work ... How on
earth are you ever going to explain in terms of
chemistry and physics so important a biological
phenomenon as first love?

–Albert Einstein

Content

Abstract

Optical sensors operating in the infrared range of the electromagnetic spectrum are key components in a variety of applications including optical communication, night vision, medical diagnosis, surveillance, and astronomy. Semiconductor nanowires have great potential for realizing broadband infrared photodetectors with excellent responsivity, low dark current and low noise, and a unique compatibility with commercial silicon-based electronics. In this thesis work, comprising three published articles in Nano Letters, we synthesized, characterized and modeled disruptive infrared photodetectors based on InP nanowires with axially embedded InAsP quantum discs. In the first article, we made a combined study of design, growth, device processing and optoelectronic properties of $n^+{-}i{-}n^+$ InP detector elements comprising 4 million periodically ordered nanowires in arrays, including either a single or 20 InAsP quantum discs. Optimized Zn compensation of the residual non-intentional n-dopants in the i-segment suppressed the dark current at room-temperature to a few pA/NW. The detector elements exhibit a strong broadband photoresponse with contributions from both the InP and InAsP segments with a threshold wavelength of about 2.0 µm and a bias-tunable responsivity reaching 7 A/W@ 1.38 µm at 2 V bias. In the second article, we performed an in-depth experimental and theoretical investigation of the responsivity of optimized photodetectors under different illumination conditions. The photodetectors exhibit strongly bias and power-dependent responsivities reaching record-high values of 250 A/W at 980 nm/20 nW and 990 A/W at 532 nm/60 nW, both at 3.5 V bias. Complementary real device modeling revealed a new photogating mechanism, induced by the complex charge carrier dynamics involving optical excitation and recombination in the quantum discs and interface traps, which reduces the electron transport barrier between the n^+-segment and the i-segment under illumination. Finally, in the last article, we demonstrate the first intersubband photocurrent response in a nanowire heterostructure array photodetector. The infrared response from 3 to 20 µm is enabled by intersubband transitions in the low-bandgap InAsP quantum discs. The intriguing optical characteristics, including unexpected sensitivity to normal incident radiation, are partly explained by excitation of the longitudinal component of optical modes in the photonic crystal formed by the nanostructured portion of the detectors. Our results show that properly designed arrays of axial nanowire heterostructures are promising candidates for realization of commercially viable broadband photodetectors.

Acknowledgment

Five years of my PhD journey has come to an end and I would like to acknowledge some of many people whose presence during the last five years have made this journey a great development experience for me, both scientifically and personally.

It is my immense pleasure to express my deepest gratitude to my main supervisor Prof. Håkan Pettersson. Thank you for giving me the opportunity to work as a PhD student in this interesting field and also for your endless support, patient guidance and useful advices. I'm grateful for all the discussions we had about different projects and for your constructive feedback. I thank you for all the knowledge and skills which I learnt from you.

I also thank my co-supervisor Prof. Lars Samuelson for creating an amazing research environment. I feel quite fortunate to have had the chance to work in such an amazing institute with excellent research equipment and knowledgeable scientists to collaborate with. Thanks for all the ideas and enthusiasm which you bring to our meetings. My sincere gratitude to my second co-supervisor Prof. Magnus Borgström for all the impressive research you are doing in your group and for all the discussions regarding growth and processing of the NW samples we have had. Your research group has always been kind enough to provide us with nanowires of excellent quality.

My profound thanks to current and former PhD students and postdocs, Vishal, Ali, Alexander, Magnus H., Xulu, Steve, Enrique, Irene, Lukas and Hossein for great collaboration on growth, fabrication, characterization and simulation of nanowire-based IR photodetectors. Thanks for all the efforts and support you put on this project.

I would also like to thank Prof. Ying Fu and Prof. Bernd Witzigmann for their collaboration and valuable inputs regarding the band structure of QDiscs-in-NW systems and electro-optical properties of corresponding detector elements. I appreciate the time you dedicated to all the skype meetings we had over and over again.

A special thanks goes to Dr. Linda Höglund from IRnova for initiating our collaboration on passivating the surface of commercial T2SL detectors. Thank you for the opportunity you gave me to work on this exciting project and I hope some good results will come out from this project.

Thank you Sudha and Sara, my officemates, for making a calm and a quiet environment in the office and for all the nice discussions we had about different topics.

A sincere gratitude to all technical, administrative and IT staff, Luke, Anders, Ivan, George, Håkan, Mariusz, Peter, Sara. A, Sarah. Mc, Natalia, Dmitry, Peter, David, Alexander, Bengt, Anna-Karin, Anastasiia, Charlotte, Gabriele, Gerda, Helena, Line, Marica, Janne and Johanna who do a great job that makes everything at FTF work just fine.

My friends and colleagues at FTF, Yang Chen, Antti, Anette, Pradheebha, Mercy, Reza, Samareh, Luna, Bahar, Mahtab, Ebrahim, Bita, Oskar, Markus, Kristi, Jonatan, Ivan, Martin, Neimantas, Sven, Therese, Sebastian, Victor, Florinda, Erik, David, Calle and Egor. It was great to know all of you. I wish you all great success in your future career and life as well.

A big hug to all my Lund Nayan Hockey teammates, Karl, Jothi and Deepika, Lena, Els, Tim, Colin, Victor, Filip, Joeri, Paul, Nils and many others. Thank you all for the great friendship we have made and for all the memorable moments we went through together during our wins and losses in the Swedish national hockey league. We keep it up!

I would like to thank all my friends outside academia, Keyvan and Reyhane, Hassan and Sima, Reza and Maryam and little Niki, Parisa, Hadi and Lisa, Roya, Saeed H., Peyman and Somayeh, Saeed P. and Ashrafi and little Delvin and all my other friends. Thank you all for your companionship and the great time we had together.

I wish to express my deepest gratitude to my family; my dad Norouz Ali, my mom Masoumeh and my sisters Nesa and Kosar. Thanks for your continuous moral and emotional support during these years. Words can't express the gratitude I feel when I think about what you have done for me. You all occupy a bright part in my mind and my heart.

My dear wife, Elena. Thank you for being there during ups and downs of my PhD, for your unconditional love and for pushing me to go after my dreams. Thank you, for being you and I love you!

Popular scientific summary

The light we can see with our eyes is a very small portion of what is known as *Electromagnetic radiation*, or *waves*. Electromagnetic waves vary across a broad range from gamma radiation used to kill cancer cells, or the x-rays used for medical imaging, to radio waves used for communication. The fundamental nature of electromagnetic radiation is oscillating, interconnected electric and magnetic waves. The main difference between the varies types of waves is the wavelength, the distance between two corresponding peaks, or troughs, in the electromagnetic fields. Infrared (IR) radiation is also an example of electromagnetic radiation, one of great technological importance. All objects in the universe emit some level of IR radiation, invisible to human eyes but sensed by us as heat, two well-known examples being the sun, and fire. Electronic devices that are sensitive to IR radiation are called IR sensors. IR sensors are key components in a variety of applications including optical communication, night vision, medical diagnosis, surveillance, and astronomy.

During my PhD, I have worked on a new class of IR sensors based on tiny nanocrystals called nanowires (NWs). Nanowires are needle-like structures, around a thousand times thinner than human hair. In our sensors, millions of connected NWs stand vertically next to each other with free space in between. Properly optimized with respect to diameter and inter-nanowire distance, these nanomaterials are excellent absorbers for IR radiation due to their antenna-like shape and matched optical properties. Moreover, the small diameter of the NWs makes it possible to combine different semiconductor materials along the NW (so called NW heterostructures), and thereby to tune their electro-optical properties. The small diameter of the NWs also potentially makes it possible to integrate NW sensors with standard commercial silicon electronics.

In my research work, I have used many different advanced techniques to fabricate and analyze IR sensors based on NW heterostructures. By embedding thin segments of different material in the NWs, we demonstrate a new class of sensors with state-of-the-art sensitivity and broadband characteristics. In order to unravel the physical mechanisms behind their excellent performance, we also carried out extensive data analysis and simulations.

I believe that the outcome of my PhD work represents a significant step forward towards understanding how to design novel commercially viable high-performance photodetectors for future smart electronic solutions.

List of papers

This thesis is based on the following articles:

I. **Room-temperature InP/InAsP Quantum Discs-in-Nanowire Infrared Photodetectors**

Mohammad Karimi, Vishal Jain, Magnus Heurlin, Ali Nowzari, Laiq Hussain, David Lindgren, Jan Eric Stehr, Irina A. Buyanova, Anders Gustafsson, Lars Samuelson, Magnus T. Borgström and Håkan Pettersson

Nano Letters 17, 3356-3362 (2017)

I performed the fabrication of the devices and optimized the processing scheme. I carried out I-V and spectrally-resolved photocurrent measurements. I also contributed to analysis of the data and wrote the paper jointly with Vishal Jain with input from the co-authors.

II. **Intersubband Quantum Disc-in-Nanowire Photodetectors with Normal-Incidence Response in the Long-Wavelength Infrared**

Mohammad Karimi, Magnus Heurlin, Steven Limpert, Vishal Jain, Xulu Zeng, Irene Geijselaers, Ali Nowzari, Ying Fu, Lars Samuelson, Heiner Linke, Magnus T. Borgström and Håkan Pettersson

Nano Letters 18, 365-372 (2018).

I performed the fabrication of the devices and carried out all optical and electrical characterization. I actively contributed to analyzing the data and wrote the paper with input from the co-authors.

III. **High Responsivity of InP/InAsP Nanowire Array Broadband Photodetectors Enhanced by Optical Gating**

Mohammad Karimi, Xulu Zeng, Bernd Witzigmann, Lars Samuelson, Magnus T. Borgström and Håkan Pettersson

Nano Letters 19, 8424–8430 (2019)

I performed the optimized fabrication of the devices and carried out all electrical and optical characterization. I actively contributed to analyzing the data and wrote the paper with input from the co-authors.

The following articles are not included in this thesis; they are however relevant to applications of NWs for optoelectronic devices in general and for photodetectors in particular:

I. Nanowire photodetectors with embedded quantum heterostructures for infrared detection

Mohammad Karimi, Magnus Heurlin, Steven Limpert, Vishal Jain, Ebrahim Mansouri, Xulu Zeng, Lars Samuelson, Heiner Linke, Magnus T. Borgström and Håkan Pettersson

Infrared Physics & Technology 96, 209-212 (2019)

II. Defect-induced Infrared Electroluminescence from Radial GaInP/AlGaInP Quantum Well Nanowire Array Light-Emitting Diodes

Laiq Hussain, Mohammad Karimi, Alexander Berg, Vishal Jain, Magnus T. Borgström, Anders Gustafsson, Lars Samuelson and Håkan Pettersson

Nanotechnology 28, 485205 (2017)

III. Optimization of current injection in AlGaInP core-shell nanowire light-emitting diodes

Pyry Kivisaari, Alexander Berg, Mohammad Karimi, Kristian Storm, Steven Limpert, Jani Oksanen, Lars Samuelson, Håkan Pettersson and Magnus T. Borgström

Nano Letters 17, 3599–3606 (2017)

IV. Bias-dependent spectral tuning in InP nanowire-based photodetectors

Vishal Jain, Magnus Heurlin, Mohammad Karimi, Laiq Hussain, Mahtab Aghaeipour, Ali Nowzari, Alexander Berg, Gustav Nylund, Federico Capasso, Lars Samuelson, Magnus T. Borgström and Håkan Pettersson

Nanotechnology 28, 114006 (2017)

V. InP/InAsP Nanowire-Based Spatially Separate Absorption and Multiplication Avalanche Photodetectors

Vishal Jain, Magnus Heurlin, Enrique Barrigon, Lorenzo Bosco, Ali Nowzari, Shishir Shroff, Virginia Boix, Mohammad Karimi, Reza Jafari Jam, Alexander Berg, Lars Samuelson, Magnus T. Borgström, Federico Capasso and Håkan Pettersson

ACS Photonics 4, 2693–2698 (2017)

Abbreviations

ALD	Atomic layer deposition
Au	Gold
BOE	Buffered oxide etch
DEZn	Diethylzinc
EBL	Electron beam lithography
EDX	Energy-dispersive X-ray spectroscopy
FDTD	Finite difference time domain
FIR	Far-infrared
FTIR	Fourier transform infrared spectroscopy
H_2SO_4	Sulfuric acid
HCL	Hydrochloric acid
InAsP	Indium arsenide phosphide
InP	Indium phosphide
ITO	Indium tin oxide
KI/I_2	Potassium iodide
LED	Light emitting diode
LWIR	Long-wavelength infrared
MBE	Molecular-beam epitaxy
MOVPE	Metalorganic vapor-phase epitaxy
MWIR	Mid-wavelength infrared
NIL	Nanoimprint lithography
NIR	Near-infrared
NPs	Nanoparticles
NW	Nanowire
PC	Photocurrent
PH_3	Phosphine
QD	Quantum dot
QDIP	Quantum dot infrared photodetector
QDisc	Quantum disc
QW	Quantum well
QWIP	Quantum well infrared photodetector
RIE	Reactive ion etching
SEM	Scanning electron microscope
SiO_x	Silicon dioxide
STEM	Scanning transmission electron microscopy
SWIR	Short-wavelength infrared
T2SL	Type-2 superlattice
Ti	Titanium
TMIn	Trimethylindium
UV	Ultraviolet

1 Introduction

Semiconductor nanowires (NWs) have been extensively studied during the last two decades due to their interesting fundamental electro-optical properties. It has been shown that NWs are promising nanoscale structures for the next generation of electrical and optical devices such as field-effect transistors[1], solar cells[2,3], diodes[4], LEDs[5,6], lasers[7,8] and photodetectors[9,10]. The small footprint of NWs leads to an efficient relaxation of strain in lattice-mismatched heterostructures and facilitates heterogeneous integration of III-V semiconductor NW devices with mainstream Si technology. Properly designed NW arrays also offer an enhanced light absorption with lower material consumption compared to planar counterparts. Embedding low-dimensional quantum heterostructures in NWs permits new degrees of design freedom for optimization of electrical and optical performance. Ultraviolet and infrared (IR) quantum discs-in-NW (QDiscs-in-NW) photodetectors[11-13], room-temperature lasers based on NWs with quantum dots[14], ultrafast photodetectors based on core-shell NWs[15] and disc-in-wire light emitting diodes[6] are some examples of NW devices with embedded quantum heterostructures.

This thesis deals with IR photodetectors based on NW arrays with embedded axial quantum heterostructures. InP NWs are grown by metalorganic vapour-phase epitaxy (MOVPE) with embedded axial InAsP quantum heterostructures called quantum discs. The combination of InP/InAsP materials is interesting for high-speed devices because these materials have excellent transport properties[16]. Also, the conduction band offset between InP and InAsP is suitable for engineering confined stated in the quantum discs to tailor the operating wavelength. Synthesizing this material system in a NW geometry combines the advantages of NWs mentioned above with bandgap tuning and confinement in quantum discs to achieve high performance IR photodetectors. Chapter 2 in this thesis presents a brief discussion of IR radiation and currently available IR photodetectors with applications. In Chapter 3, we describe the growth, fabrication and characterization of InAsP/InP QDiscs-in-NW photodetectors. In Chapter 4, we describe the development of the processing steps for fabrication of high-performance photodetectors comprising 4 million vertically standing NWs, connected together with a low-resistance transparent top contact, with a high collection efficiency of photogenerated carriers. This work found an undesired self-gating effect induced by the oxide and transparent top contact coatings, which resulted in a radial MOS-like depletion which modulates the distribution of carriers in the NWs under bias. To resolve this, the nanofabrication steps were optimized by introducing an extra step to fill the space between the NWs with a polymer. Also, it is demonstrated that unintentional n-doping in NWs deteriorates the performance of the photodetector because it increases the dark current. To compensate this unintentional doping, we introduce Zn in the nominally intrinsic region which, together with an improved processing scheme and an increased number of quantum discs, resulted in high-performance room-temperature photodetectors with a cut-off wavelength of about 2 μm. In Chapter 5, we look into the physics behind the very high responsivity exhibited by the photodetectors and reveal an optical gating effect induced by recombination of photogenerated holes with electrons trapped by surface defects and quantum discs. Finally, in Chapter 6, we demonstrate a broadband photoresponse from 3 to 20 μm at low temperature, which we primarily attribute to intersubband transitions between the ground state and the first excited state of the embedded InAsP quantum discs. Interestingly, the detectors were sensitive to normal incident radiation, in sharp contrast to planar quantum well infrared photodetectors (QWIPs). Supported by detailed optical modeling, we interpret this observation partly in terms of excited longitudinal components of optical modes in the photonic crystal formed by the nanostructured portion of the detectors. The thesis is concluded with a summary and outlook in Chapter 7.

2 Infrared detector technologies and applications

In this chapter, we briefly discuss the basics of IR radiation and its important applications. Then, the technologies currently employed for detecting IR radiation will be presented, followed by a motivation for using NWs as IR detector elements.

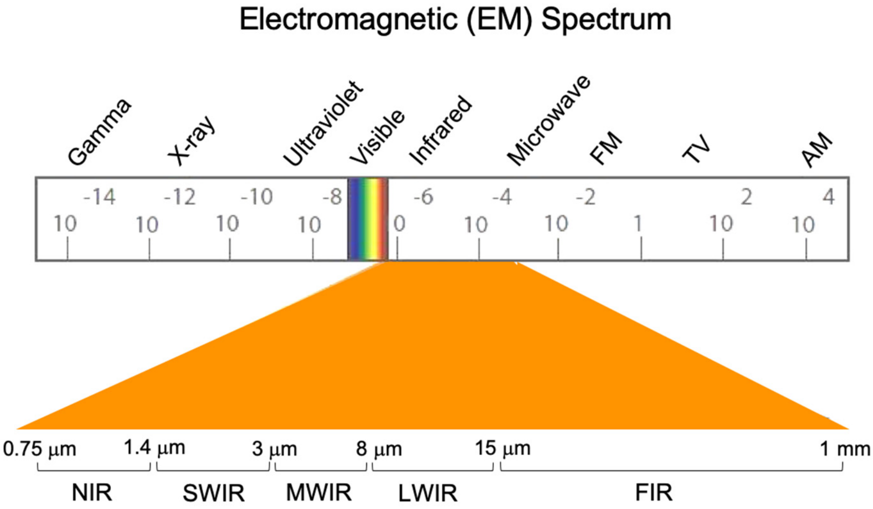

Figure 2.1 Electromagnetic spectrum with the IR region highlighted.

2.1 Infrared radiation

The IR region is defined as the electromagnetic (EM) spectral range between the visible and millimeter wavelengths corresponding to about 0.75-1000 μm (Figure 2.1). The invisible IR radiation was first discovered in 1800 by William Herschel when he dispersed solar light through a prism and measured the temperature of the different colors using a thermometer with blackened bulbs. The warmest range, subsequently denoted IR, was found beyond the red spectrum. Infrared radiation is emitted by all objects and it is related to their temperature. Objects with a temperature higher than 1000 K primarily emit in the visible wavelength region, while cooler bodies, such as the human body, emit in the IR region.

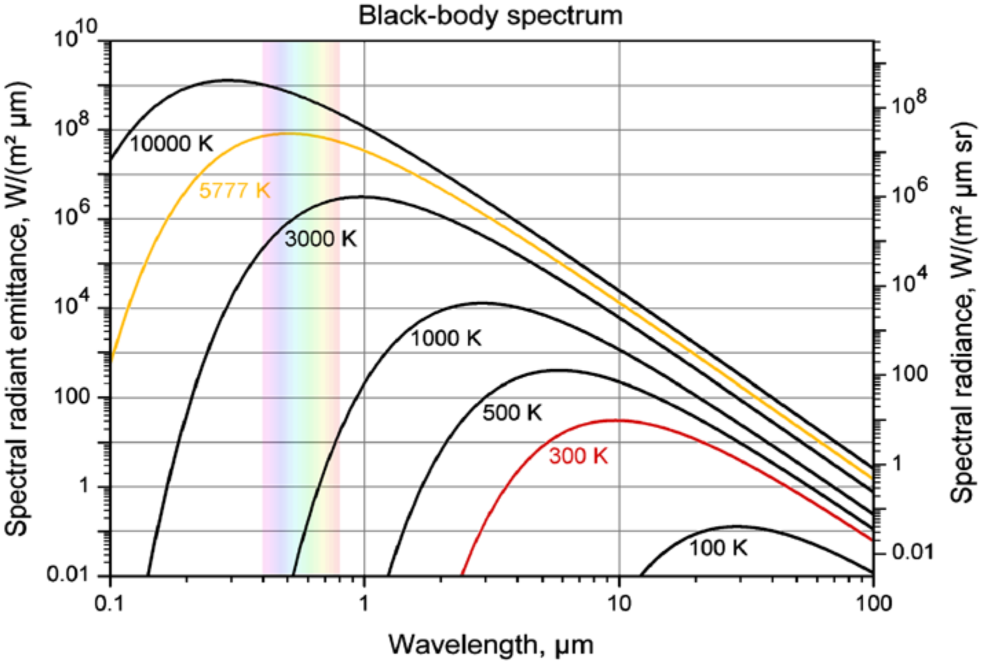

Figure 2.2 Spectral irradiance of a black body as a function of wavelength[17]

The correlation between spectral irradiance of a body and its temperature was theoretically explained by the German physicist Max Planck by introducing the concept of energy quanta, a seminal contribution to physics for which he was awarded the Nobel Prize in Physics in 1918. A blackbody is an ideal physical object that absorbs all incoming electromagnetic radiation, regardless of the frequency or incident angle, reflecting or transmitting none. The emitted spectral irradiance, $I(\lambda, T)$, from a perfect blackbody radiator is given by Planck´s famous radiation law[18]:

$$I(\lambda, T) = \frac{2\pi hc^2}{\lambda^5}\left[exp\left(\frac{hc}{\lambda kT}\right) - 1\right]^{-1}, \qquad (2.1)$$

where λ is the wavelength, T is the temperature, h is Planck’s constant, c is the velocity of light, and k is Boltzmann’s constant. Figure 2.2 shows the black body radiation as a function of wavelength for various temperatures. For example, an object with a temperature of 300 K displays a peak emission at around 12 µm. The peak emission wavelength shifts toward shorter wavelengths as the temperature of the body increases.

The IR range is often subdivided into the following five regions:

- Near-infrared (NIR, 0.75 – 1.4 µm)
- Short-wavelength infrared (SWIR, 1.4 – 3 µm)
- Mid-wavelength infrared (MWIR, 3 – 8 µm)
- Long-wavelength infrared (LWIR, 8 –15 µm)
- Far infrared (FIR, 15 µm – 1 mm)

NIR and SWIR have many applications e.g. in optical communication, reflectography, surveillance and optical coherence tomography. MWIR and LWIR, which are also known as 'thermal infrared', have many military surveillance applications as well as civilian applications including environmental monitoring, industrial process control and medical screening. Infrared radiation in the FIR region is used e.g. in astronomy, long-wavelength heaters and in medical therapy.

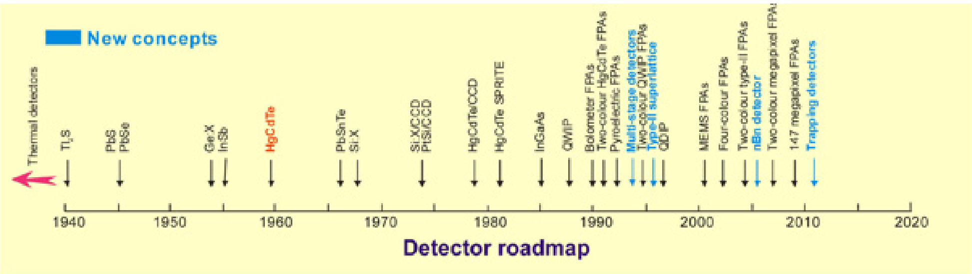

Figure 2.3 Chronology of significant development of IR detectors[19]. HgCdTe detector alloys were demonstrated as early as 1959[20]. The concepts of quantum well infrared photodetectors[21] (QWIPs) and quantum dot infrared photodetectors[22] (QDIPs) were introduced in 1987 and 1998, respectively.

2.2 Classification of IR photodetectors

Infrared detectors in general can be classified into two groups: thermal detectors and photon detectors. In thermal detectors, the output signal depends on the change of temperature of the detector element resulting from the absorbed power of the incident radiation. Thermal detectors are thus not selectively sensitive to the photon energy. The Golay cell, thermistor bolometer and thermopile are examples of thermal detectors. While typically working at room-temperature, this kind of detector is usually characterized by a low sensitivity and slow response speed. In photon detectors, the output signal is proportional to the number of incident photons and thus wavelength dependent. These devices offer high response speeds and high sensitivity in comparison to thermal detectors. Photon detectors are usually cooled if the operation wavelength is longer than 3 μm[23] to reduce thermal excitation of carriers which would otherwise result in a poor signal-to-noise ratio. Significant developments of IR detectors and systems in chronological order is displayed in Figure 2.3[19]. Early IR photon detectors were based on lead sulfide (PbS), operating in the 1.3–3 μm range and mostly used for military applications. In the early 1950s, compounds of InAs and InSb were developed to detect IR radiation; however, the operation wavelength window was limited to 3–5 μm. The need to extend the detection range to long IR wavelengths led to the development of HgCdTe detectors in the late 1950s. These materials have been the basis of IR detectors for many years

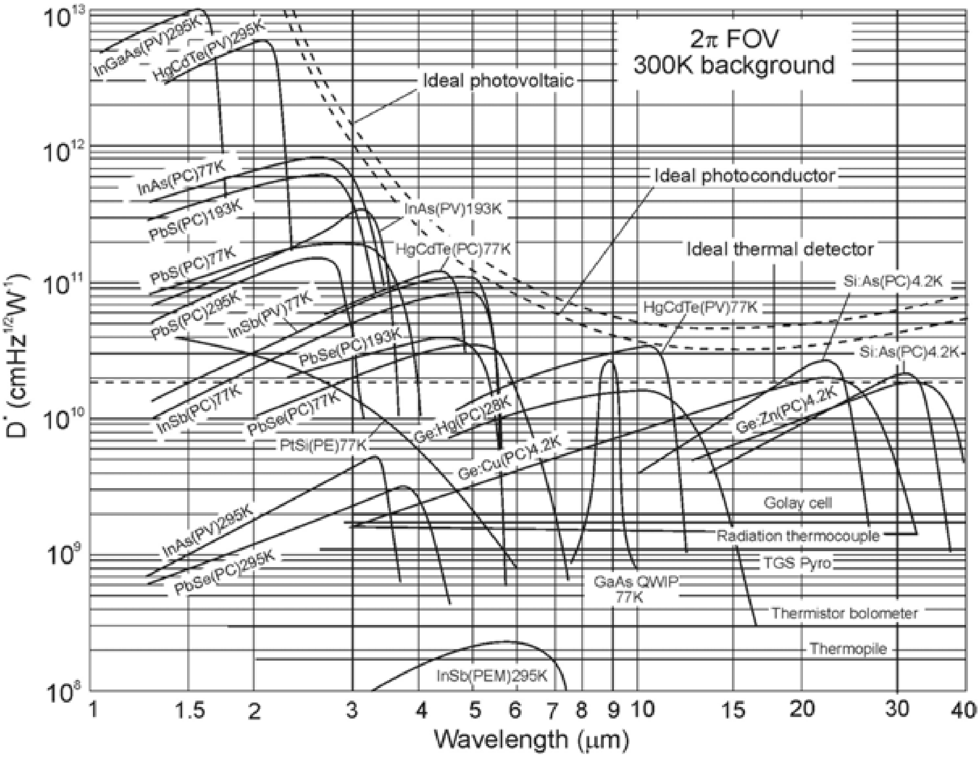

Figure 2.4. Specific detectivity (D^*) of various commercial IR photodetectors as a function of wavelength for a given operating temperature[24]. A chopper frequency of 1000 Hz is used for all detectors except for the thermopile, thermocouple, thermistor bolometer, Golay cell and pyroelectric detector which were all used with a chopper at 10 Hz. The detectors are assumed to have a 2π field of view at a temperature of 300 K. The dashed lines indicate theoretical limits for the background-limited D^* for ideal photoconductive detectors, photovoltaic detectors and thermal detectors.

due to their high sensitivity and spectral tunability. The difficulties associated with growing high-quality HgCdTe materials, related to a large solidus-liquidus separation and a high vapor pressure of Hg, led to the introduction of novel IR detector architectures. Intersubband photodetectors, such as quantum well IR photodetectors (QWIPs) and quantum dot IR photodetectors (QDIPs), were developed to overcome the long-wavelength cut-off of most conventional photodetectors. There have been great efforts made to develop detectors that work in the MWIR and LWIR, as the atmospheric transmission is high in these spectral windows. Type-II superlattice detectors[25,26], nBn[27,28] detectors, photon trapping detectors and multi-stage/cascade infrared devices are some other examples of emerging detector technologies. Figure 2.4 summarizes the performance of various commercially available IR photodetectors in terms of specific detectivity[24]. In the following section, we briefly discuss a few examples of currently available IR photodetectors.

2.2.1 The *p-n* photodiode

Photodiodes are common semiconductor photodetectors containing a *p-n* junction and often an intrinsic segment between the p-type and n-type regions. Incoming radiation with photon energies larger than the bandgap is absorbed in the depletion region (including the intrinsic segment) where it generates electron-hole pairs (EHPs) which in turn are separated and swept away by the built-in electric field. The electrons and holes are collected by the electrical contacts forming a photocurrent which is proportional to the intensity of the absorbed light over a wide range of optical powers. Photodiodes can be operated in three different modes. In the photovoltaic mode, also known as the zero-bias mode, the detector produces a measurable photocurrent proportional to the intensity. In the photoconductive mode, a reverse bias is applied to the device which increases the width of the depletion region (and thus the absorption volume) leading to a bias-dependent photocurrent. The operation mode of photodiodes at high electric field strengths close to breakdown is called the avalanche mode. Under avalanche conditions, the photogenerated charge carriers in the depletion region gain a kinetic energy sufficiently large to induce more EHPs via impact with the host atoms in the crystal. In this way, a single electron generated in the depletion region can result in the generation of many more, resulting in a detector gain.

2.2.2 HgCdTe photodetectors

$Hg_{1-x}Cd_xTe$ (MCT) is a chemical compound of cadmium telluride (CdTe) and mercury telluride (HgTe). HgTe is a semimetal with a bandgap of 0 eV, while CdTe is a semiconductor with a bandgap of about 1.5 eV at room temperature. By changing the amount of Cd in the alloy, the bandgap can be thus be tuned between 0 and 1.5 eV (i.e. from SWIR–LWIR). HgCdTe alloys have been widely used materials for detection of MWIR and LWIR radiation in *p-i-n* photodetectors via interband transitions. The adjustable direct bandgap, a high absorption coefficient, a moderate thermal coefficient of expansion and a moderate dielectric constant are some of the advantages of this material in photodetector[29] applications. However, there are also some disadvantages associated with this material system. First, adjusting the cut-off wavelength in ternary alloys with large band gap differences is difficult because mole fraction control is challenging. Second, HgCdTe alloys suffer from non-uniform growth and high defect densities. Also, a high Auger recombination rate in these materials reduces the signal-to-noise ratio and affects the room-temperature operation of the photodetector. In addition, in contrast to QWIPs and QDIPs, HgCdTe-based photodetectors do not offer bias-tunable multi-color detection capabilities in contrast to QWIPs and QDIPs.

2.2.3 Photoconductors

One of the most well-known properties of bulk semiconductors is the increase of electrical conductivity with incident optical power. The simplest type of photodetector consists of a semiconductor slab supplied with two highly doped end contacts. The incident radiation induces a change in the conductivity of the semiconductor, which can be monitored as a photocurrent for an applied bias. The quantum efficiency, excess carrier lifetime and transit time through such a photoconductor are important parameters that determine the magnitude of the photocurrent[30]. In contrast to *p-n* junctions discussed above, a photoconductor thus requires an external bias to provide a detector signal. Planar semiconductor photodetectors with incorporated quantum structures, such as quantum wells and quantum dots, are well-known examples of photoconductors. The basic operating principles of these photodetectors are given in the following two sections. Also, NW photoconductors is an expanding research field due to their unique electro-optical properties.[31,32] In this thesis, we report on NW photoconductors with embedded quantum heterostructures that offer a dramatically extended sensitivity window. More details about these structures and detector geometries will be given in Chapters 4 and 5.

2.2.4 Quantum well infrared photodetectors

Advances in developing new methods for growing high quality semiconductor compounds with well controlled composition and stoichiometry, such as molecular beam epitaxy (MBE), metalorganic chemical vapour deposition (MOCVD) and chemical beam epitaxy (CBE), have enabled scientists to design and synthesize disruptive nanoscaled structures for emerging electronics and photonics. The concept of QWIPs is based on sandwiching a low bandgap semiconductor in between two wider bandgap semiconductors[33]. If the width of the low bandgap semiconductor is thin enough, the energy levels in both the conduction band and valence band will be quantized due to confinement leading to formation of intersubband levels. Since these energy levels depend on the quantum well thickness, band offsets and effective mass of the carriers, the spacing between these levels can be tailored by altering the composition and thickness of the well to match the desired IR wavelength window. Various semiconductor compounds such as GaAs/AlGaAs, InGaAs/InAlAs, InSb/InAsSb, InAs/GaInSb and SiGe/Si have been proposed and studied for use as a basic material for QWIPs. Figure 2.5 shows the schematic layout and corresponding conduction band profile of a typical GaAs/AlGaAs QWIP under bias. The incident radiation excites an electron in the ground state of the quantum well to the excited state from which the electron subsequently escapes to the barrier matrix through a combination of thermal excitation and quantum tunneling. The excited carriers are collected by the applied electric field which forms the detector signal. While the schematic QWIP in Figure 2.5 comprises only three quantum wells, commercial QWIPs often contain tens of stacked quantum wells.

QWIPs offer excellent performance characteristics which distinguish them from other IR detectors. Due to a high uniformity of the epitaxial growth over large areas, QWIPs are suitable candidates for large scale production systems. Also, the fabrication of QWIPs is easier than MCT detectors due to the use of manufacturing techniques that are standard for III-V semiconductors[34]. Moreover, QWIPs offer low dark current and multicolor detection capability by combining various materials with different compositions and/or thicknesses matching the detection band to the desired photon wavelengths. The spectral sensitivity window can also be tuned by the external applied bias via the Stark effect. There are also drawbacks to QWIPs, including a low absorption coefficient due to the thin quantum well layers. This, together with the short lifetime of intersubband transitions and competing thermal excitation of charge carriers results in a poor performance at elevated temperatures and it becomes necessary to integrate the QWIPs with bulky mechanical Stirling coolers. Another limitation of the QWIPs results from the optical selection rules for intersubband transitions dictated by the quantum mechanical nature of the confined states. The optical absorption in quantum wells strongly depends on the polarization of the incoming photons. Optical matrix elements determine the probability for a transition between an initial state and a final state. The matrix element for a two-state system can be written as follows:

$$\langle f\boldsymbol{k}'|\boldsymbol{e}.\widehat{\boldsymbol{p}}|i\boldsymbol{k}\rangle = \int \psi^{*}_{f\boldsymbol{k}'}(\boldsymbol{r})\boldsymbol{e}.\widehat{\boldsymbol{p}}\,\psi_{i\boldsymbol{k}}(\boldsymbol{r})d^{3}\boldsymbol{r} \qquad (2.2)$$

where f and i describe the wave function (ψ) in the final and initial states with corresponding wave vectors $\mathbf{k'}$ and $\mathbf{k}$, respectively. **e** represents the polarization vector and $\hat{\boldsymbol{p}}$ is the momentum operator equal to $-i\hbar\nabla$. Considering a quantum well with a quantization along the z-direction, the total wavefunction can be described as the product between an envelope function $\phi(z)$ and a plane wave in the **r**=(x,y) plane

$$\Psi_{ik}(\boldsymbol{r}, z) = A^{-\frac{1}{2}}\phi(z)\exp(i\boldsymbol{kr}), \qquad (2.3)$$

where A is introduced to properly normalize the wavefunction. If the incoming light is polarized in the x-direction, $\boldsymbol{e}.\hat{\boldsymbol{p}}$ becomes -i$\hbar$ ∂/∂x.This operator will only affect the plane wave, with no effect on the envelope function. Consequently, the matrix element (Eqns. 2.2 and 2.4) will be zero, as the i and j states are mutually orthogonal to each other, implying that there will be no intersubband absorption for any polarization in the x-y plane.

$$\langle f\boldsymbol{k}'|\hat{p}_x|i\boldsymbol{k}\rangle = \hbar k_x\langle f\boldsymbol{k}'|i\boldsymbol{k}\rangle = 0 \qquad (2.4)$$

However, if the light is polarized in the z direction, the momentum operator will change to -i$\hbar$ ∂/∂z which will affect the envelope function of the bound state. Hence, the matrix element will be given by:

$$\langle f\boldsymbol{k}'|\hat{p}_z|i\boldsymbol{k}\rangle = 1/A\int dz\int d^2\boldsymbol{r}\ \phi_f^*(z)e^{i(\boldsymbol{k}-\boldsymbol{k}')\boldsymbol{r}}\hat{p}_z\,\phi_i(z) \qquad (2.5)$$

The integral over r is zero, except for the case when k′ is equal to k. Then, the integral in Eqn. 2.5 can be written as follows:

$$\langle f|\hat{p}_z|i\rangle = -i\hbar\int \phi_f^*(z)\frac{\partial_{\phi_i(z)}}{\partial_z}dz \qquad (2.6)$$

This implies that the matrix element for light polarized in the z-direction is not zero, due to the large overlap between the wavefunction of the excited state and the derivative of the wavefunction of the ground state, and an intersubband transition can thus occur. From this follows that the transition from an odd to an even energy state is most probable, while the transition between two even, or two odd energy states has vanishing probability.

Due to the dependence of the optical absorption on the polarization of the incoming light, QWIPs must be irradiated at some angle to properly couple the IR radiation into the detector element. In practice, 45° polished facets or diffraction gratings are used to redirect the normally-incident radiation into the active region of the QWIP. QWIPs have been extensively studied since their invention, both theoretically and experimentally. Several review articles and books related to QWIPs have been published[35,36]. Nowadays, QWIPs form the basic detector elements in large focal plane arrays with excellent uniformity[37] and performance.

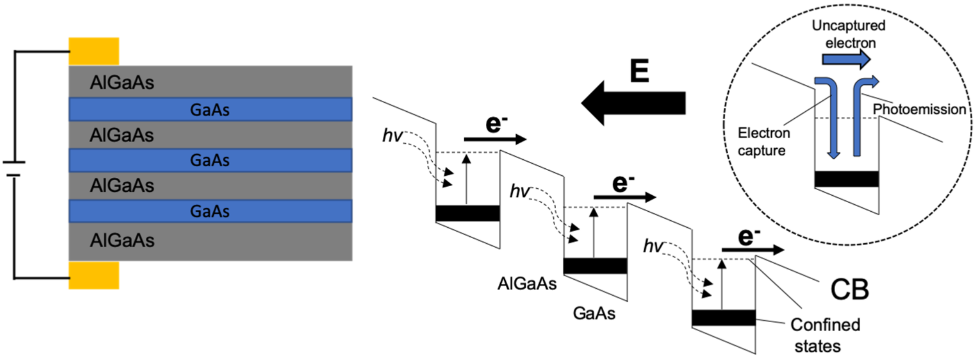

Figure 2.5 Schematic of a typical GaAs/AlGaAs QWIP (left) with the corresponding conduction band profile and intersubband excitation under bias (right).

2.2.5 Quantum dot infrared photodetectors

Photocurrent generation in QWIPs is strongly polarization dependent as a result of the optical selection rules for quantum wells as discussed above. Quantum dot (QD)-based photodetectors do not have this limitation due to relaxed selection rules resulting from the three-dimensional confinement in QDs. The so-called Stranski–Krastanow (S-K) growth mode is usually used to synthesize QDs from thin lattice mismatched epitaxial layers[38]. The elastic energy of a thin epitaxial layer grown on top of a substrate with typically smaller lattice constant increases with the layer thickness. Above a certain critical thickness that depends on the lattice mismatch, a spontaneous relaxation of the stored elastic energy takes place by a redistribution of the material in the epilayer to a fairly uniform ensemble of strain-relaxed QDs on top of a thin wetting layer. Similar to QWIPs, QDIPs typically comprise many stacked QD layers on top of each other[39]. Quantum dot layers are usually doped to populate the ground states with electrons. Similarly to QWIPs, these carriers can be optically excited in intersubband transitions to excited states, similar to QWIPs, from which they eventually escape to the conduction band where they are collected by an electric field to form a photocurrent[40].

Three main advantages of QDIPs are[41]:

1) Sensitivity to normally-incident IR radiation. Intersubband absorption may occur for normal incidence radiation, in contrast to QWIPs due to different absorption selection rules. Normal incidence absorption in QDIPs has been reported by several groups[42-44].
2) The signal-to noise ratio in QDIPs is typically enhanced in comparison to QWIPs. Due to three-dimensional quantization in QDs and the phonon bottleneck effect, the carrier lifetime is enhanced[45].
3) Reduced dark current. The thermal emission of electrons from the ground state of the QDs is expected to be reduced compared to QWIPs due to the three-dimensional quantum confinement in the QDs.

The first optical intersubband transition in quantum dots was reported in 1989 for InSb QDs[46]. Since then, various materials have been the subject of research for QDIPs, including InGaAlAs on InP, InSb on GaSb and GaAs, InGaAs on Si, Ge on Si, and InGaAs on InGaP. The main disadvantage associated with QDIPs is the non-uniformity of the QDs, resulting in a broadening and shift of the absorption spectrum. This makes tailoring of the operation detection window of the QDIPs challenging[47,48]. To further enhance the operation performance of QDIPs, it has been suggested to embed the QDs in QW structures. These so-called QD-in-well infrared photodetectors offer new degrees of freedom for adjustment of the spectral sensitivity window and for optimization of the operation temperature. Since the optical transitions take place between energy levels in the QDs and QW, the operation wavelength can be tailored to the desired IR window by changing the size and composition of the QDs and QW[49], respectively.

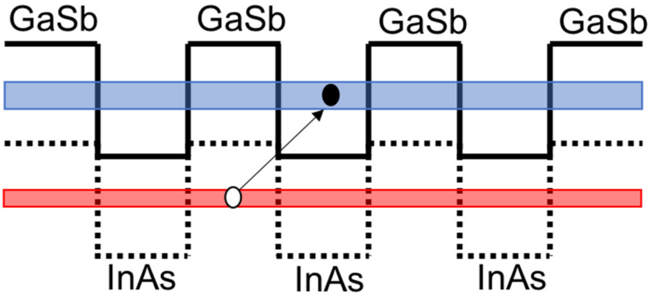

Figure 2.6 Schematic band alignment of a typical InAs/GaSb T2SL.

2.2.6 Type-II superlattice infrared photodetectors (T2SLs)

Type-II broken bandgap superlattices (T2SLs) comprise thin semiconductor heterostructures, where both the conduction band and valence band edges of one semiconductor are below the valence band edge of the second semiconductor[50-52] (Figure 2.6). By growing periodic structures comprising alternating thin layers with this band alignment it is possible to create artificial minibands for electrons and holes that are sensitive to optical transitions. In contrast to QWIPs and QDIPs, where the IR response is based on intersubband transitions, the detection mechanism in T2SLs[53,54] is based on optical transitions between the minibands. InAs/GaSb is a commonly used heterostructure for MWIR and LWIR T2SLs. Surface currents have historically been the limiting factor for these detectors, but recent advances in surface passivation has mitigated this problem. Current state-of-the-art T2SLs are typically limited by Shockley-Read-Hall (SRH) recombination via mid-gap defects. The possibility to reduce Auger recombination in these materials allows the devices to operate at elevated temperatures.[55]

Table 2.1 Comparison of IR detectors[45]

Detector Type			Advantages	Disadvantages
Thermal (thermopile, bolometers, pyroelectric)			Light, rugged, reliable, and low cost. Room-temperature operation	Low detectivity at high operation frequency Slow response
Photon	Intrinsic	IV–VI (PbS, PbSe, PbSnTe)	Easy to fabricate Highly stable materials	Very high thermal expansion coefficients Large permittivity
		II–VI (HgCdTe)	Easy bandgap tailoring Multicolor detectors Well-developed theory	Non-uniform over large area High cost for growth and processing
		III–V (InGaAs, InAs, InSb, InAsSb)	Reliable material & dopants Advanced monolithic integration possible	Heteroepitaxy with large lattice mismatch Long wavelength cutoff limited to 7 μm (at 77 K)
	Extrinsic	(Si:Ga, Si:As, Ge:Cu, Ge:Hg)	Very long wavelength operation Relatively simple fabrication process	High thermal generation rate Very low temperature operation only
	Type-I Quantum wells (GaAs/AlGaAs, InGaAs/AlGaAs)		Mature material growth Good uniformity over large areas Multicolor capability	High thermal generation rate Complicated design and growth Sensitive to polarization
	Quantum dots (InAs/GaAs, InGaAs/InGaP, Ge/Si)		Normal incidence sensitivity Reduced thermal generation	Complicated design and growth. Issues with non-uniform size of QDs.
	Type-II Superlattices (InAs/InGaSb, InAs/InAsSb)		Low Auger recombination rate Easy wavelength control	Complicated design and growth Sensitive to the interfaces

All the photodetectors discussed in this chapter have their own advantages and disadvantageous as briefly discussed above and summarized in Table 2.1. QWIPs are sensitive to light only polarized in the growth direction. QDIPs suffer from non-uniformities in size and shape of the QDs which lead to a broadening of the detection window. T2SLs require a precise control of the growth of defect-free thin layers and advanced passivation procedures. HgCdTe-based photodetectors contain toxic elements and they also suffer from non-uniformity issues which makes the fabrication of large-area photodetectors challenging. High-performance HgCdTe detectors are expensive and typically implemented only in military applications[56]. Another general disadvantage with all of the detectors discussed above is that they cannot be directly integrated with mainstream mature Si technology due to high lattice-mismatch.

3 Nanowire-based IR photodetectors

It is expected that the worldwide mid-IR sensor market of $9.7 billion in 2018 will increase to about $110 billion by 2025. Such a huge investment together with the limitations associated with the currently available commercial photodetectors have encouraged development of novel kinds of IR detectors. The general trend of continuously decreasing dimensions for electronic devices in accordance with the *More than Moore* concept has propelled the research in IR nanophotonics. However, becasue light absorption has a direct relationship with the dimensions of the active device volume, the smaller the dimensions, the smaller the absorption. Several methods have been suggested to enhance the photon absorption such as resonant cavities and plasmonic enhanced photodetectors[57] which all add complexities in terms of fabrication and device integration leading to expensive devices[58].

Semiconductor nanowires (NWs) have been shown to be potential nanoscale candidates for addressing all of the issues related to existing photodetectors. Nanowires are low-dimensional structures with a length of the order of microns and diameters ranging from tens to hundreds of nanometers. They have been intensively investigated during the last two decades, offering new ways of designing and fabricating various types of semiconductor devices including e.g. photodetectors, LEDs[59,60], lasers[61,62], solar cells[2,63], transistors[64] and tunnel diodes[65]. In particular, the bottom-up approach for synthesis of NWs has opened up the possibility to realize disruptive NW-based electronics and photonics. Owing to their small foot print, epitaxial growth of III-V NWs on Si substrates is readily facilitated[66], and so high performance optoelectronics can be merged with mainstream silicon technology. Another reason for the rapid development of the NW field is the possibility of incorporating highly lattice-mismatched axial heterostructures with sharp interfaces in NWs which is not possible in a thin-film geometry[67-69]. Scientists at Nanolund have been pioneers in developing high performance electronic and photonic devices. The NW-based solar cell with 13.8 % efficiency exceeding the ray optics limit[2], a particle-exchange (PE) heat engine based on embedded InAs quantum dots in InP NWs[70], vertical InAs/InGaAsSb/GaSb NW tunnel FETs with the ability to operate well below 60 mV/decade[64] and continuous aerosol-based growth of NWs with controlled nanoscale dimensions[71] are just some examples of recognized breakthroughs (Figure 3.1).

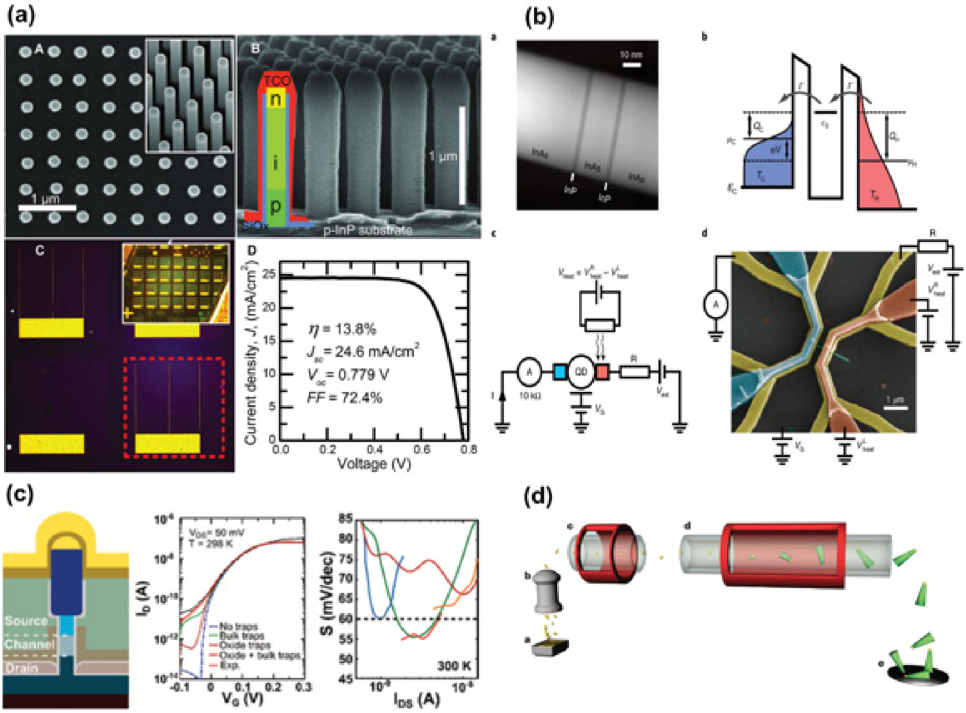

Figure 3.1 (a) NW-array solar cells with 13.8 % efficiency[2]. (b) A quantum dot heat engine operating close to the thermodynamic efficiency limits[70]. (c) Nanowire tunnel field-effect transistors operating below 60 mV/decade[64]. (d) Continuous gas-phase synthesis of NWs with tunable properties[71].

The unique photonic features of NWs make them an excellent candidate for optical sensors. The possibility to fabricate highly ordered arrays of NWs with fine-tuned diameter and pitch facilitates a high absorption with small material volume due to an efficient coupling of the incoming radiation to the optical modes of the NW array. It has e.g. been shown that with a proper design of InP NW arrays, solar cells can deliver 83% of the photocurrent density of planar InP solar cells, while only 12% of the surface is covered by NWs. Moreover, the added advantage of synthesized axial and radial heterostructures, combined with monolithic compatibility with Si substrates, open up interesting opportunities for photodetector applications. There has been a remarkable progress on developing NW-based photodetectors during the last two decades. Single InP NWs with a responsivity of 3000 A/W[72], single InGaAs NWs operating in the range of 1100 – 2000 nm with a responsivity of 6.5×10^3 A/W[73], single GaAsSb/GaAs heterostructure NWs operating in the range of 1100 – 2200 nm with the responsivity of 1.05×10^3 [74] and ensembles of InAs NWs on Si operating in the range 1.4 – 3.3 µm[75] are just a few examples. Most of the research associated with NW-based photodetectors has been focused on single NW structures. Issues related to growing high-quality NW arrays with excellent yield over large areas, together with serious hindrances for vertical processing of large arrays, have so far led to limited success in terms of realizing high-performance array photodetectors. Furthermore, the inclusion of low-dimensional quantum heterostructures in NWs adds new degrees of design freedom for optimization of electrical and optical performance. To the best of our knowledge, there are only a few reports regarding NW array photodetectors with embedded quantum heterostructures[76,77]. Also, despite the rapid pace of NW photodetector development, there have been no reports to date of intersubband photocurrent generation in NWs which is essential for detection of long wavelength radiation. Table 3.1 summarizes the reported performance of photodetectors based on arrays of NWs.

Table 3.1 Performance characteristics of NW-based array photodetectors[56].

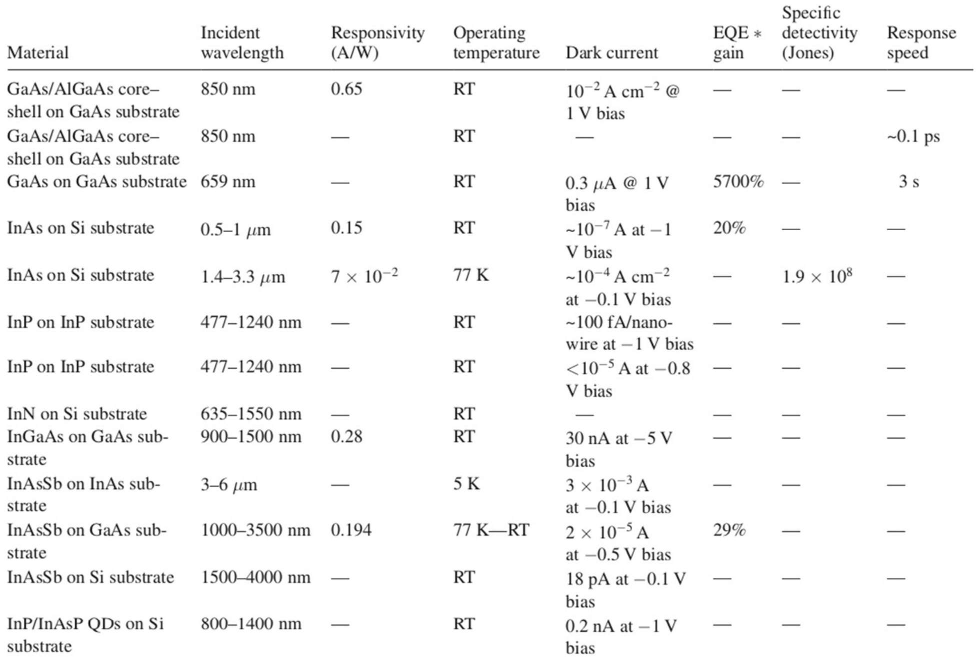

Material	Incident wavelength	Responsivity (A/W)	Operating temperature	Dark current	EQE * gain	Specific detectivity (Jones)	Response speed
GaAs/AlGaAs core–shell on GaAs substrate	850 nm	0.65	RT	10^{-2} A cm^{-2} @ 1 V bias	—	—	—
GaAs/AlGaAs core–shell on GaAs substrate	850 nm	—	RT	—	—	—	~0.1 ps
GaAs on GaAs substrate	659 nm	—	RT	0.3 μA @ 1 V bias	5700%	—	3 s
InAs on Si substrate	0.5–1 μm	0.15	RT	~10^{-7} A at −1 V bias	20%	—	—
InAs on Si substrate	1.4–3.3 μm	7×10^{-2}	77 K	~10^{-4} A cm^{-2} at −0.1 V bias	—	1.9×10^{8}	—
InP on InP substrate	477–1240 nm	—	RT	~100 fA/nanowire at −1 V bias	—	—	—
InP on InP substrate	477–1240 nm	—	RT	<10^{-5} A at −0.8 V bias	—	—	—
InN on Si substrate	635–1550 nm	—	RT	—	—	—	—
InGaAs on GaAs substrate	900–1500 nm	0.28	RT	30 nA at −5 V bias	—	—	—
InAsSb on InAs substrate	3–6 μm	—	5 K	3×10^{-3} A at −0.1 V bias	—	—	—
InAsSb on GaAs substrate	1000–3500 nm	0.194	77 K—RT	2×10^{-5} A at −0.5 V bias	29%	—	—
InAsSb on Si substrate	1500–4000 nm	—	RT	18 pA at −0.1 V bias	—	—	—
InP/InAsP QDs on Si substrate	800–1400 nm	—	RT	0.2 nA at −1 V bias	—	—	—

In this thesis work, we report on InP NW array photodetectors with embedded InAsP quantum heterostructures. InP/InAsP heterostructures are of particular interest for high-speed optoelectronic devices because of their excellent transport properties. The relatively large conduction band offset in the InP/InAsP system strongly confines carriers leading to higher operating temperatures and lowers the leakage current in detectors. While typically a p^+-i-n^+ geometry is chosen for interband detectors, we focus on an n^+-i-n^+ geometry, in combination with incorporated InAsP quantum discs (QDiscs), since we ultimately target broadband detectors offering both interband and intersubband photodetection capabilities. We first optimize design, growth and fabrication of visible-SWIR interband photodetectors to obtain excellent performance at room-temperature. Then we further investigate the photoconductive gain of the detectors to unravel the physics behind the remarkably high responsivity. Also, we report on the first spectrally resolved photodetector in a NW array geometry with a normal incidence photoresponse in the LWIR/FIR region, resulting from intersubband transitions in the embedded QDiscs.

3.1 Nanowire growth

A number of techniques have been developed to synthesize high-quality semiconductor NWs. These techniques can generally be categorized into one the following approaches: bottom-up or top-down. The top-down approach uses different patterning and etching techniques to form semiconductor NWs from bulk crystals. The smallest NW thickness in this case is limited by the resolution of the lithography system and the etching characteristics. Besides the drawbacks with complicated processing issues, it is also generally not possible to fabricate NW heterostructures of highly lattice-mismatched materials such as InP/InAs using the top-down approach. In the bottom-up approach, a NW is formed by epitaxial layer-by-layer growth. This method provides explicit control of the NW composition and length during growth. Heterostructure NWs with large lattice mismatch can be grown using the bottom-up method due to strain relaxation resulting from the small diameter (footprint) of the NWs. Also, in-situ n and p-doping of the NWs facilitates fabrication of photodiodes, photoconductors, LEDs and lasers.

Metal-organic vapor phase epitaxy (MOVPE) is the most commonly used method for epitaxial growth of NWs and more generally the preferred method for mass production of optoelectronic devices such as solar cells, laser diodes, LEDs and photodetectors[78]. MOVPE relies on the formation of solid crystals from a vapor phase of different precursor gases. For growth of InP NWs, the group III element indium (In) is supplied via the precursor trimethylindium (TMIn) contained in a liquid form in a bubbler. A carrier gas, such as hydrogen (H_2), flows through the bubbler and dissolves some of the TMIn precursor molecules and transfers them to the growth chamber. The group V element phosphorous (P) is directly supplied in a gas phase by the precursor phosphine (PH_3).

In order to grow NWs using MOVPE, metal seed nanoparticles (NPs), often made of gold (Au), are used as catalysts. The NPs are in a liquid form at typical growth temperatures of 400-500°C. An efficient collection by the NPs of the constituent elements required for growth facilitates an enhanced nucleation rate at the boundary between the particle, vapor and solid (the so-called V-L-S mechanism) producing a rapid (nm/s) layer-by-layer growth. A detailed explanation of the NW growth theory is beyond the scope of this thesis.

Three main methods are mainly used to produce and arrange NPs. One fast and cheap method is based on an aerosol technique, which results in a randomized arrangement of the NPs on the substrate surface. However, a precise arrangement of well-defined NPs is essential as eventually the NW pitch, length and diameter (roughly equal to the NP diameter) govern the optical properties of the NW arrays. Electron-beam lithography (EBL) has proven to be a good alternative to the aerosol technique that provides precise control over the shape, size and position of the NPs[79]. Another useful technique for generating NPs with similar quality properties as those made by EBL, and also with much higher throughput is nanoimprint lithography (NIL). In this method, an intermediate polymer stamp is used to transfer the pattern of NPs to a resist layer deposited on a substrate under specific thermal and UV illumination conditions.[80]

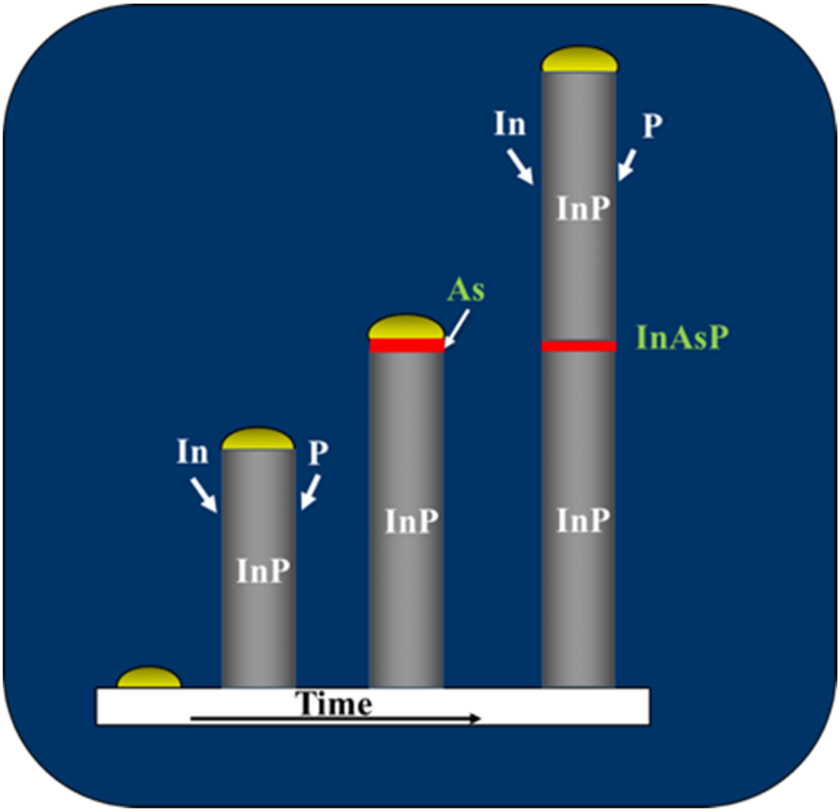

Figure 3.2 Different schematic steps for growth of InP NWs with an embedded InAsP QDisc. First Au NPs are patterned using NIL, then In and P precursors are introduced into chamber to grow InP NWs. For growth of nominal InAs (in reality InAsP) QDiscs, the P supply is switched off, As is introduced into the chamber and In is supplied from the NP. Finally, In and P precursors are again introduced to grow the upper InP section.

For growth of the NWs discussed in this thesis, n^+-InP (111)B substrates were patterned with Au particles using NIL, metal evaporation, and lift-off. The final pattern consisted of 20 nm-thick Au discs with a diameter of 180 nm, which during growth formed 130 nm diameter Au−In alloy particles. The center-to-center distance (pitch) between two Au particles was 400 nm. The growth was carried out in a low-pressure (100 mbar) Aixtron 200/4 MOVPE at 440 °C. The grown NWs had a diameter of 130 nm and a length of about 2 µm. Embedded axial nominal InAs QDiscs were grown by turning off the trimethylindium (TMIn) flow and replacing the phosphine (PH_3) with arsine (AsH_3) for 1 or 2 s. In this so-called deplete mode growth of QDiscs, stored In is supplied from the NPs instead of being supplied by the precursor gas. Figure 3.2 shows schematically the growth of InAsP/InP QDisc-in-NWs. Figure 3.3 shows a typical scanning electron microscope (SEM) image of the grown NW arrays.

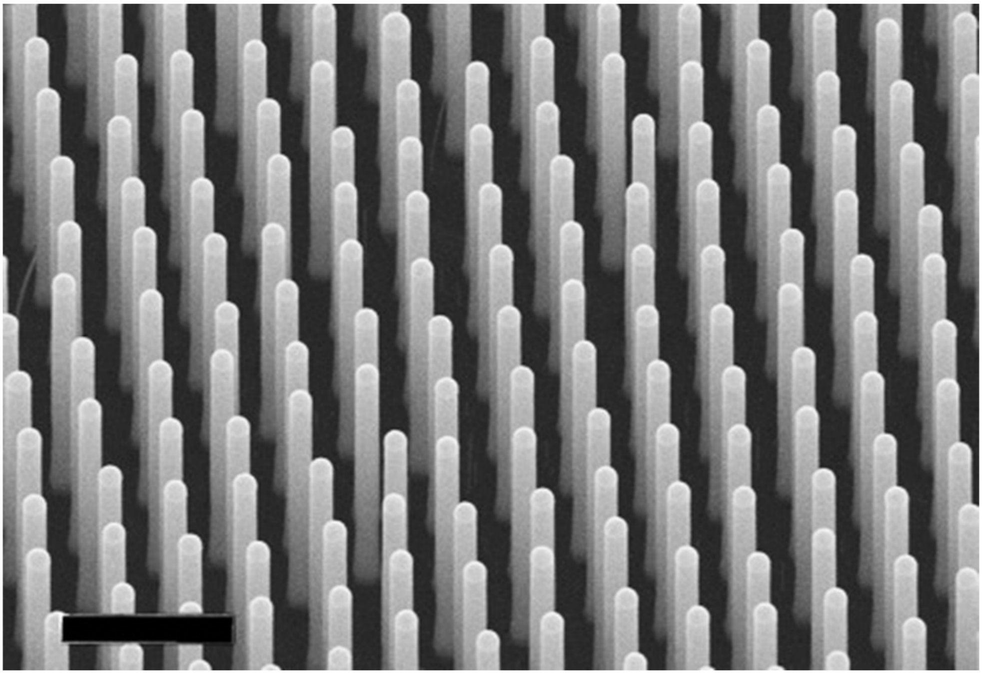

Figure 3.3 SEM image of a grown InAsP/InP QDiscs-in-NW array. The scale bar is 1 µm.

3.2 Fabrication of NW array photodetectors

After growing the NWs using MOVPE, a series of processing steps are used to make NW-based photodetectors. In general, the substrate is used as the back contact while the tips of the NWs, connected together by an ITO film, are used as the top contact. To separate these contacts from each other, first an insulating SiO_2 layer is homogenously deposited on the as-grown samples using atomic layer deposition (ALD). This insulating layer covers all parts of the NWs and the substrate in between the NWs. To make the top contact, the insulating layer should be removed from the tip of the NWs. For this purpose, a thick photoresist S1818 is spun on the sample to completely embed the NWs. A step-wise back etching of this resist is subsequently performed using reactive ion etching (RIE) to reveal the very tips of the NWs. When a desired length of the NWs is exposed, the SiO_2 layer is removed from the tips using a buffered oxide etchant (BOE). The gold catalyst NPs are also removed in this step using a KI/I_2 solution. After removing the remaining resist using wet etching, the device areas are defined by UV lithography step.

In order to connect the exposed tips of the NWs, a 50 nm thick indium tin oxide (ITO) layer is sputtered on the sample as a transparent top contact. Prior to the sputtering step, any native oxides were removed using an H_2SO_4/H_2O (1:10) solution to avoid a potentially poor contact formation between the NWs and ITO. After this step, another spinning resist and lithography step is used to remove the ITO from non-device areas using an HCl solution. Finally, the bond pads are defined by a third UV lithography step followed by evaporation of Ti and Au layers. For initial IV measurements, the sample is glued to a copper coin. After selection of the best devices based on these initial IV measurements, the sample is mounted on a 14-pin DIL holder for in-depth optoelectronic characterization. Different steps of the complete processing chain are shown in Figure 3.4.

The following sections discuss each of these fabrication steps in more details.

3.2.1 Deposition of insulating SiO_2 layer

The first step in the processing of NW arrays is to deposit a homogenous insulating layer of SiO_2. The deposition is carried out using tri(tert-butyl) silane (TTBS) and trimethylaluminium (TMA) as precursors in a Savannah 100 ALD system. To deposit thicker layers, the ALD system is operated in exposure mode in which the pump is blocked while introducing precursors into the chamber. This method gives sufficient time for the precursors to fully diffuse around the sample providing better uniformity over high-aspect ratio geometries. The deposition is carried out through the self-limiting rapid SiO_2 ALD technique using TTBS, while Al obtained from the TMA acts as a catalyst (ALD Savannah 100 & 200 user manual)[81]. The deposited layer (~50 nm) is thus not pure SiO_2 in composition, but contains intermixed Al. Furthermore, an additional thin (<5 nm) layer of Al_2O_3 is deposited as an adhesive layer since resists used in the subsequent process steps do not adhere well to SiO_x which can lead to undesired oxide etching. A SEM image of NWs coated with an insulating layer of SiO_x is shown in Figure 3.5.

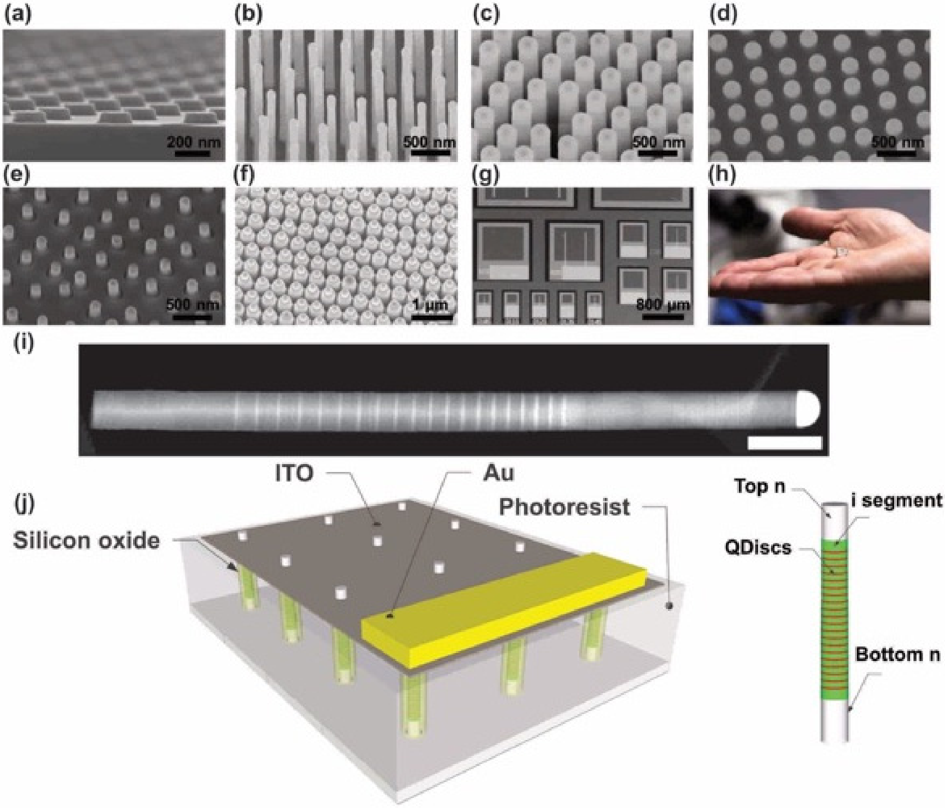

Figure 3.4 An overview of different processing steps to make NW array photodetectors. (a) Definition of Au seed particles by nanoimprint lithography (NIL). (b) Growth of InP/InAsP NWs using MOVPE. (c) Capping of the grown NWs by a SiO_x layer using atomic layer deposition (ALD). (d) Embedding of the NWs in a thick photoresist (S1818) layer and subsequent back-etching to expose 300 nm of the NW tips. (e) Etching of SiO_x and Au particles from the tips. (f) Sputtering of 50 nm ITO on top of the NWs as a transparent contact. (g) Definition of device areas using UV lithography, followed by deposition of 400 nm thick gold bond pads. (h) Sample mounted on a DIL holder and bonded for optoelectronic characterization. (i) TEM image of a single NW revealing the 20 axial InAsP QDiscs (scale bar is 200 nm). (j) Schematic of the finalized NW array detector.

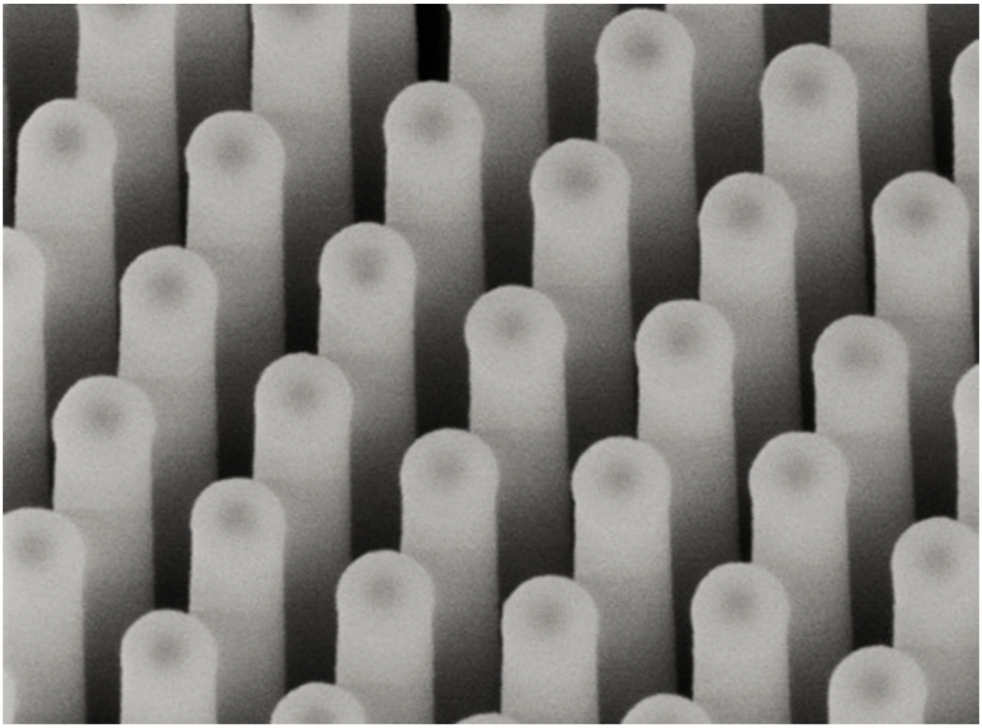

Figure 3.5 NWs after depositing an insulating SiOx layer

The homogenously deposited insulating layer should be removed from the tips of the NWs in order to fabricate the top contact. The sample is covered by a thick resist (S1818) layer using spinning speeds which give a resist thickness larger than the NW height. After soft-baking at 115°C for 90 s, the resist is step-wise back-etched using a RIE Trion T2 system. An oxygen plasma with 50W RF power and a 15 sccm O_2 flow rate at 300 mTorr pressure gives an etching rate of about 1 nm/s. The samples are checked with a Leo 1560 SEM after each RIE step using a low acceleration voltage (~10 keV electron energy) to avoid charging during imaging, as well as hard-baking of the resist. Upon achieving the desired exposed length, the SiO_x/Al_2O_3 layer is etched using a buffered oxide etch ($BOE:H_2O$, 1:10) which gives an etch rate of about 2.7 nm/s for SiO_x and about 1 nm/s for Al_2O_3. In the same step, the Au NP on the top of the NWs is also etched using KI/I_2 for 20 s which eliminates the formation of a potential Schottky barrier between the NPs and NWs[82]. An additional benefit of the NP removal is the reduction of optical reflection from the Au NPs. Finally, the resist is stripped off using acetone. Exposing the NW tips, followed by etching of the insulating layer and Au NPs is shown in Figure 3.6.

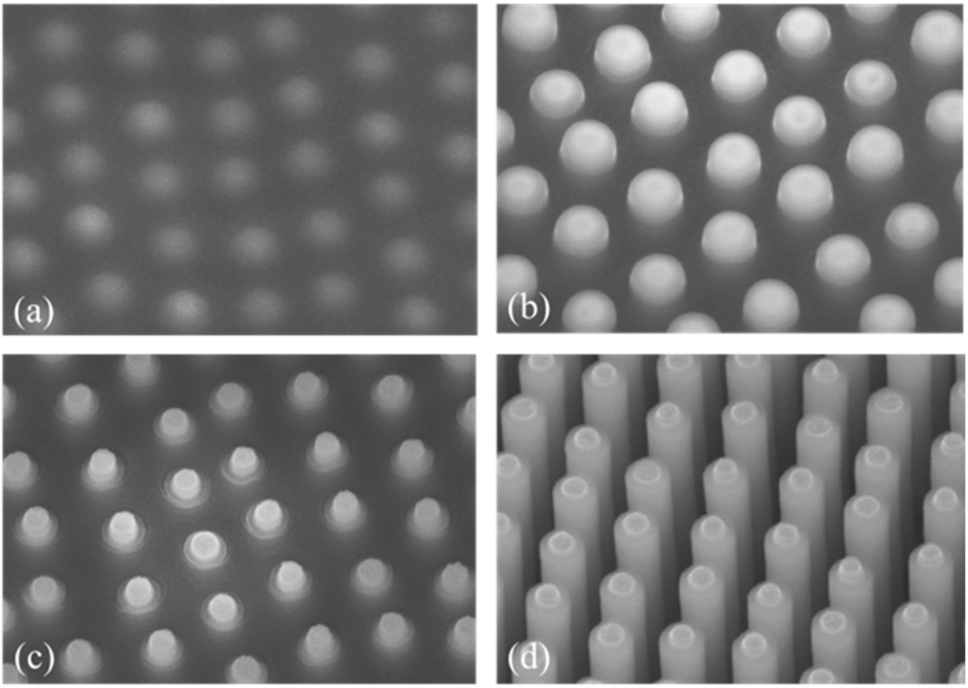

Figure 3.6 Process steps for removal of the insulating layer from the tips of the NWs. (a) Spinning a thick photoresist infill to cover the NWs. (b) Back-etching of the photoresist using RIE. (c) Etching of of SiO_x and Au NPs from the tips of the NWs, respectively. (d) Stripping of the photoresist using acetone.

3.2.2 Definition of device areas using UV lithography

In this step, the photodetector elements are defined by UV lithography. The UV exposure was performed using an MJB4 mask aligner with a 365 nm optical filter in constant power (350 W) mode with an intensity of about 22 mW/cm^2. The details of this processing step are described below.

1) The positive resist S1828 is spun at 3000 rpm for 60 s which yields a thickness of about 3.5 µm.
2) The resist residues on the sample's backside are removed using acetone.
3) The resist is soft-baked for 90 s at 115 °C.
4) The UV exposure is performed for 24 s using an appropriate mask to define the device area.
5) The sample is developed in MF 319 for 90 s, followed by rinsing in DI for 120 s.

6) The resist is then hard-baked on a hot plate for 10 min. while the temperature is increased to 200 °C. Sample is left at 200 °C for 30 min and then left to cool down on the switched-off hot plate for 10 min.

3.2.3 Sputtering of indium tin oxide top contact

After defining the device area elements, all of the tips of the NWs need to be connected in parallel to form the top contact. Indium tin oxide (ITO) has been shown to be a good option for connecting the tips due to its high conductivity properties as well as low absorption over a broad wavelength range. We use an AJA Orion sputter deposition system to sputter ITO. Prior to sputtering, any native oxide on the surface of the NWs must be removed to avoid any poor contact formation. Then the samples are immediately mounted on the sample holder and loaded into the sputterer. 150 nm sputtered ITO yields a NW sidewall coverage of about 50 nm. A UV lithography step covers the device elements, after which ITO is etched from non-device areas. Finally, the resist is removed using acetone.

The step-by-step procedure is as follows:

1) The native oxide on the NW tips is removed using a 1:10 H_2SO_4:H_2O solution for 60 s, followed by rinsing in H_2O for 60 s.
2) The sample is then immediately mounted on the sample holder and loaded into the sputterer.
3) 150 nm of ITO is sputtered using an Ar plasma with a flow of 4 sccm at 50 W RF power (Figure 3.7 a).
4) The positive resist S1813 is spun on the sample at 3000 rpm for 60s.
5) The resist is soft-baked for 90 s at 115 °C.
6) The UV exposure is performed for 7 s using an associated mask for etching ITO.
7) The sample is developed in MF 319 for 90 s, followed by rinsing in DI for 120 s.
8) ITO is etched using a 1:2 HCl:H_2O solution for 120 s.
9) Verification of the deposited ITO layer under an optical microscope (Figure 3.7 b).

3.2.4 Definition of Ti/Au bond pads

In the final step, Ti and Au are evaporated on the defined bond pad area of the devices forming the contacts to the external measurement setups. The Ma-N 490 photoresist was chosen for the lithography process which gives a resist thickness of at least 5 µm at a spinning speed of 6000 revolutions per minute (rpm). A 15 nm thick Ti layer was deposited by evaporation prior to Au deposition to facilitate the adhesion of Au to the sample.

The step-by-step procedure is as follows:

1) The samples are cleaned in acetone & IPA (120 s each) followed by drying with a N_2 gun.
2) The negative resist ma-N 490 is spun on the samples at 6000 rpm for 60 s.
3) The resist residues on the sample's backside are carefully removed using acetone.
4) The sample is then baked on a hot plate at 95 °C for 150 s and left to cool in air for 60 s.
5) The sample is mounted on the mask-aligner along with the suitable mask pattern for the negative photoresist. After wedge-error compensation (WEC) and alignment check, single cycle exposure is done for 30 s in soft-contact mode.
6) The exposure leads to cross-linking in the exposed areas of the negative resist. The remaining resist is removed using the developer ma-D 332/S for 180 s, followed by rinsing in deionized (DI) water for 120 s and N2 blow dry. Around 150 s was sufficient for the development, while an extra 30 s was crucial for obtaining about 1.5–2 µm undercut for subsequent lift-off.
7) The samples are then mounted on the sample holder in the AVAC evaporation system and pumped. After obtaining a pressure lower than 10–6 mbar, 10 nm Ti and 200 nm Au are evaporated while continuously rotating the sample for a uniform coverage.
8) For the final lift-off, the samples are placed in a beaker with acetone at 50 °C for 30 min. A mild blow of acetone solution through a pipette might be needed to stir the solution and aid in lifting-off of all the resist/Au residues (Figure 3.7 c).

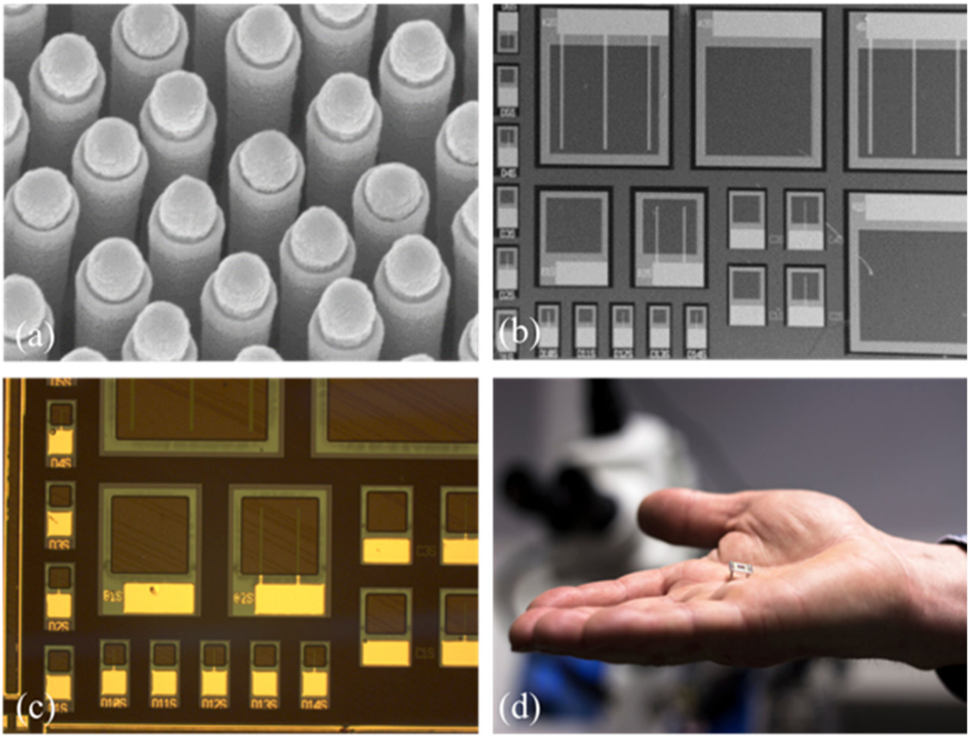

Figure 3.7 An overview of steps involved in fabrication of the top contact. (a) Sputtering of ITO to connect the tips of the NWs. (b) SEM image of device elements after sputtering and etching of ITO in non-device areas, followed by a UV lithography step to open the bond pad areas. (c) Optical microscope image of the device elements after evaporation of Ti and Au. (d) Mounted sample on a 14-pin DIL holder for optoelectronic measurements.

After this step, the samples are ready for optoelectronic characterization. For initial measurements, the sample is glued to a copper coin and for in-depth optoelectronic measurements the sample is mounted on 14-pin DIL holder (Figure 3.7 d). In the next section an overview of our optoelectronic characterization techniques will be given.

3.3 Characterization techniques

In this section, we briefly discuss the techniques and setups we used to characterize the NWs and the photodetectors made from them.

3.3.1 Photoluminescence spectroscopy

In a typical photoluminescence (PL) spectroscopy experiment, a semiconductor is illuminated with a laser with photon energies higher than the bandgap. The incoming photons excite electrons from the valence band to the conduction band forming electron-hole pairs. The excited charge carriers relax to the band edges and finally recombine. Recombination can take place radiatively by emitting a photon corresponding to the bandgap minus the binding energy of the exciton, or non-radiatively through defect states or surface states. Photoluminescence is a very useful method for investigation of electronic transitions through the spectral position, linewidth and lineshape of the recorded optical signal.

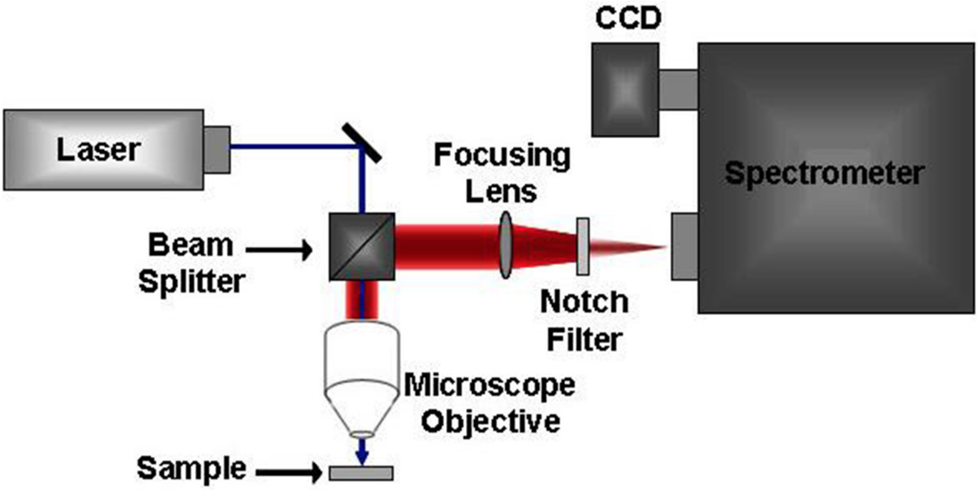

Figure 3.8 Schematic of a typical PL setup

A typical PL setup (Figure 3.8) consists of a laser excitation source with an attenuator to vary the intensity. The laser beam passes through a beam-splitter and a microscope objective which in our setup focuses the beam to a spot size smaller than 5 μm. A sample holder mounted on an X-Y stage inside the cryostat facilitates spatially flexible, low-temperature micro-PL measurements on single NWs. The PL from the sample is collected by the same objective lens and focused onto the entrance slit of a monochromator. The unwanted laser light is blocked by a notch filter. Upon entering the monochromator unit through the slit, the PL is first collimated by a mirror and then diffracted by a grating. The diffracted PL is then focused and dispersed over an InGaAs detector. On aligning the sample (NW) parallel to the vertical pixel array of the InGaAs detector, spatial photoluminescence information can also be gathered. Finally, the detector and the monochromator are coupled to a computer, which records the signal.

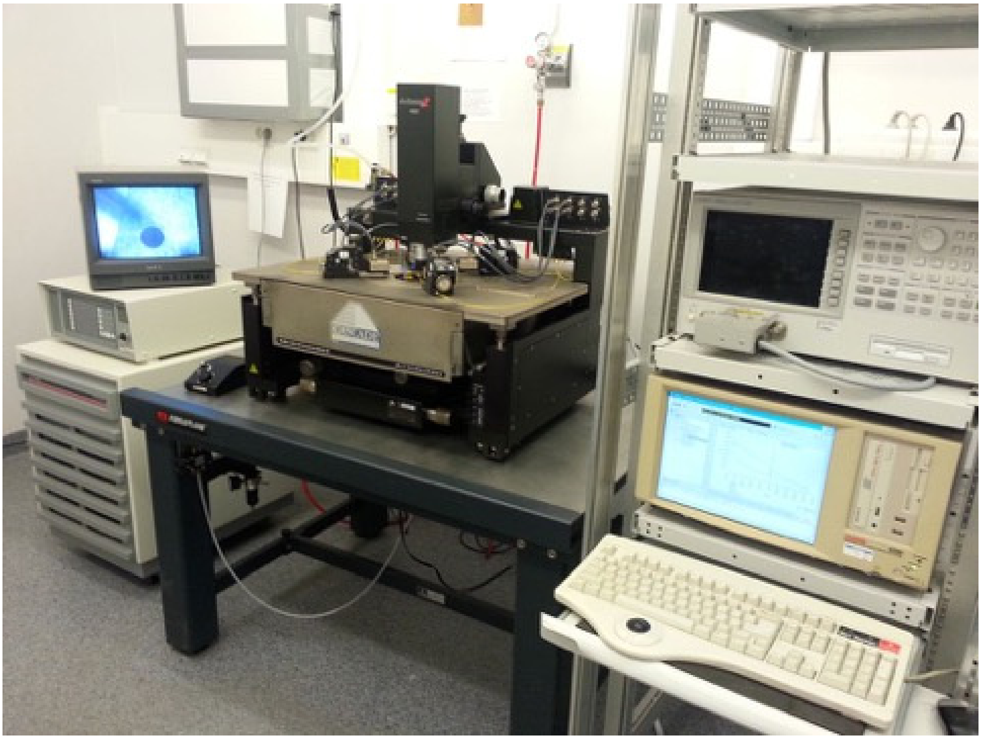

Figure 3.9 Probe station - Cascade 11000B setup at Lund University for initial IV characterization

3.3.2 Probe station measurements

The most fundamental electrical characterization of any kind of electronic device is its current-voltage (I-V) characteristics. I-V measurements recorded under dark and illuminated conditions at different temperatures provide important information about the overall performance of the device under test, as well as of the detailed transport and photogeneration mechanisms. The sheer amount of measurement work required to characterize different devices in a sample chip demands a flexible and rapid technique to measure different devices. Wire bonding is a robust method of contacting devices but is quite limited in terms of flexibility. Using probes directly contacted to the device pads to measure I-V characteristics is a much faster and flexible approach. In addition, the chuck which acts as the sample holder can also be used as the back-contact. We have used the Cascade 11000B probe station with a Keithley 4200 semiconductor characterization system for the electrical measurements. The tungsten probes were controlled with a 3D micrometer stage to position them accurately on the bond pads with the help of an optical microscope. Figure 3.9 shows the probe station setup used for initial I-V characterization.

3.3.3 Fourier transform infrared spectroscopy

Fourier transform infrared (FTIR) spectroscopy is a powerful technique capable of measuring spectrally resolved absorption, transmission, PL and photocurrent with a high signal-to-noise (SNR) ratio. Unlike a dispersive instrument where a single wavelength is used in each measurement interval, FTIR spectrometers utilizes a broadband light source containing the full spectrum of wavelengths. The source light beam shines into a Michelson interferometer where it is split into two beams using a beam-splitter, one reflected from a fixed mirror and the other from a continuously moving mirror (Figure 3.10) producing a path difference (retardation). The two beams subsequently merge where they interfere constructively or destructively, depending on the position of the moving mirror and wavelength, resulting in a modulated beam comprising all wavelengths coded by the scanning mirror. This beam is then focused onto the sample which in our case is mounted in a cryostat integrated into the sample compartment of the FTIR. The modulated light beam produces a modulated photocurrent which is amplified by a fast current-voltage amplifier. The modulated output voltage versus mirror position (interferogram) is subsequently converted to a spectrally resolved photocurrent by the well-known Fourier transform algorithm. In our measurements, we have used the FTIR model Vertex 80v from Bruker for photocurrent measurements. The spectrometer is equipped with a Janis PTSHI-950-FTIR pulse tube closed-cycle cryostat for low temperature (down to 5K) measurements. For NIR measurements, a tungsten halogen lamp is used as broadband light source, along with a CaF_2 beam splitter, while for longer wavelengths a MIR source along with a KBr beam splitter is used. The sample itself is used as a detector. The modulated photocurrent from the sample is amplified using a Keithley 428 programmable current amplifier. Figure 10 shows the schematic of our FTIR setup.

We also use the FTIR setup for temperature-dependent I-V measurements, both with and without illumination (using the spectrometer's built-in light source). The instrumentation for recording I-Vs include the Keithley models 2636B and 6430, respectively. Also, frequency-dependent photocurrent measurements for different laser irradiations (532 nm and 980 nm) were investigated using an SR830 lock-in amplifier in conjunction with an optical chopper. Figure 3.11 shows the experimental setup used for optoelectronic characterization in this thesis work.

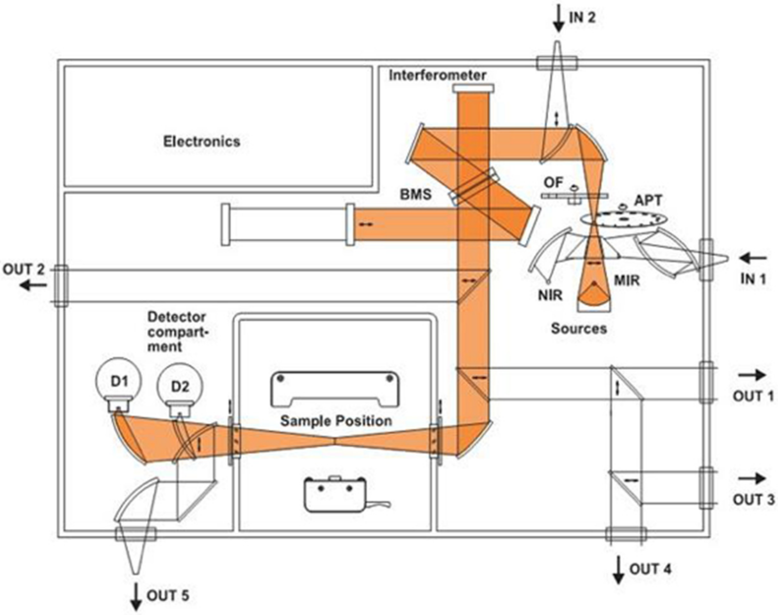

Figure 3.10 Top view schematic of our Bruker Vertex 80v FTIR setup. The cryostat (not shown) is integrated into the sample compartment (the square marked by “Sample Position” in the figure).

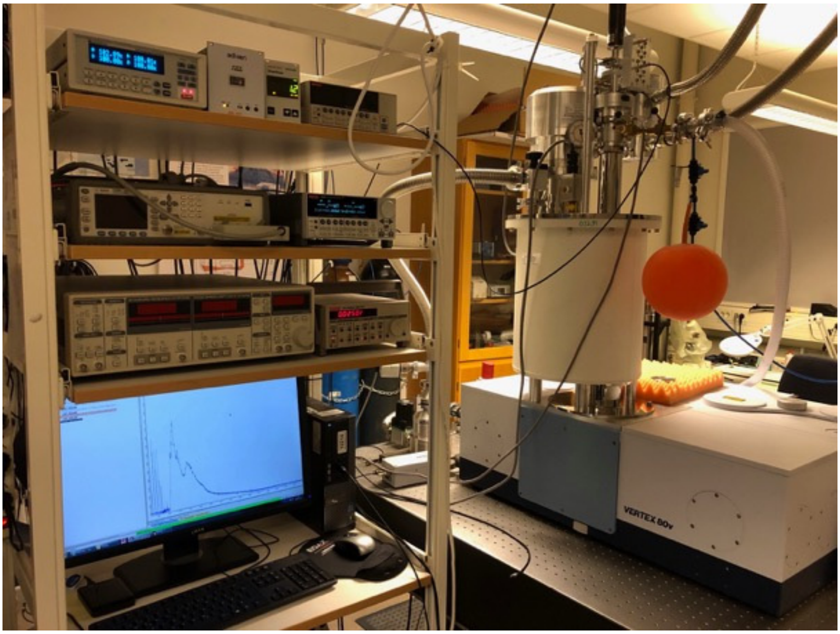

Figure 3.11 The experimental setup at the Rydberg Core Labs (RCL) at Halmstad University used for electrical and optical characterization, including FTIR spectrometer with integrated closed-cycle cryostat.

4 Interband InAsP/InP quantum discs-in-nanowire photodetectors

In this chapter, we discuss the performance of arrays of InP NWs with axially embedded single or multiple InAsP QDiscs for NIR/SWIR detection based on interband transitions. First, a detailed study of two different nanofabrication schemes was carried out in order to find the optimum method for processing of NW array detectors comprising a single QDisc in each NW. Subsequently, the number of QDiscs was increased to 20 to enhance the interband photocurrent (PC) signal. We found that the unintentional n-doping in the intrinsic section of the NWs contributes significantly to the dark current in the detectors. To compensate this unintentional n-doping, in-situ Zn doping was added to the intrinsic region. Results show that this compensation doping leads to a drastically reduction in the dark current by about four orders of magnitude, yielding excellent room-temperature detector performance with a cut-off at 2µm.

4.1 Optimization of dark current and processing scheme

It is known that InP NWs are unintentionally n-doped with a carrier concentration ranging from 10^{15} to 10^{16} cm^{-3} when grown by MBE and MOVPE[83,84]. This unintentional doping in the intrinsic region will affect the performance of the photodetector by increasing the dark current. To eliminate this effect, we used Zn as compensation doping. First a series of single QDisc-in-NW samples were grown with varying diethylzinc (DEZn) molar fractions of $\chi_{DEZn}= 0.5 \times 10^{-7}$, 1.4×10^{-7} and 4.1×10^{-7}, respectively, added during growth of the nominally intrinsic segments. InP NWs with a single InAsP QDisc were grown on n^{+}-InP (111)B substrates in a similar to that discussed in section 3.1. We processed the samples according to the procedure described in section 3.2, resulting in a photodetector shown schematically in Figure 4.1 a. I-V measurements showed that the sample grown with $\chi_{DEZn}= 0.5\times10^{-7}$ exhibited a 100-fold higher resistivity than the sample grown without χ_{DEZn}. While the two samples grown with $\chi_{DEZn} = 1.4 \times 10^{-7}$ and $\chi_{DEZn} = 4.1 \times 10^{-7}$ showed even higher resistivity (Figure 4.1 c), they also exhibited an open-circuit voltage under illumination. A probable reason for this is an overcompensation of the unintentional n-doping in the i-segment, creating an n^{+}-p^{-}-n^{+} structure instead of an n^{+}-i-n^{+} structure. Based on these results, $\chi_{\mathrm{DEZn}} = 0.5 \times 10^{-7}$ was selected as the optimum DEZn molar fraction.

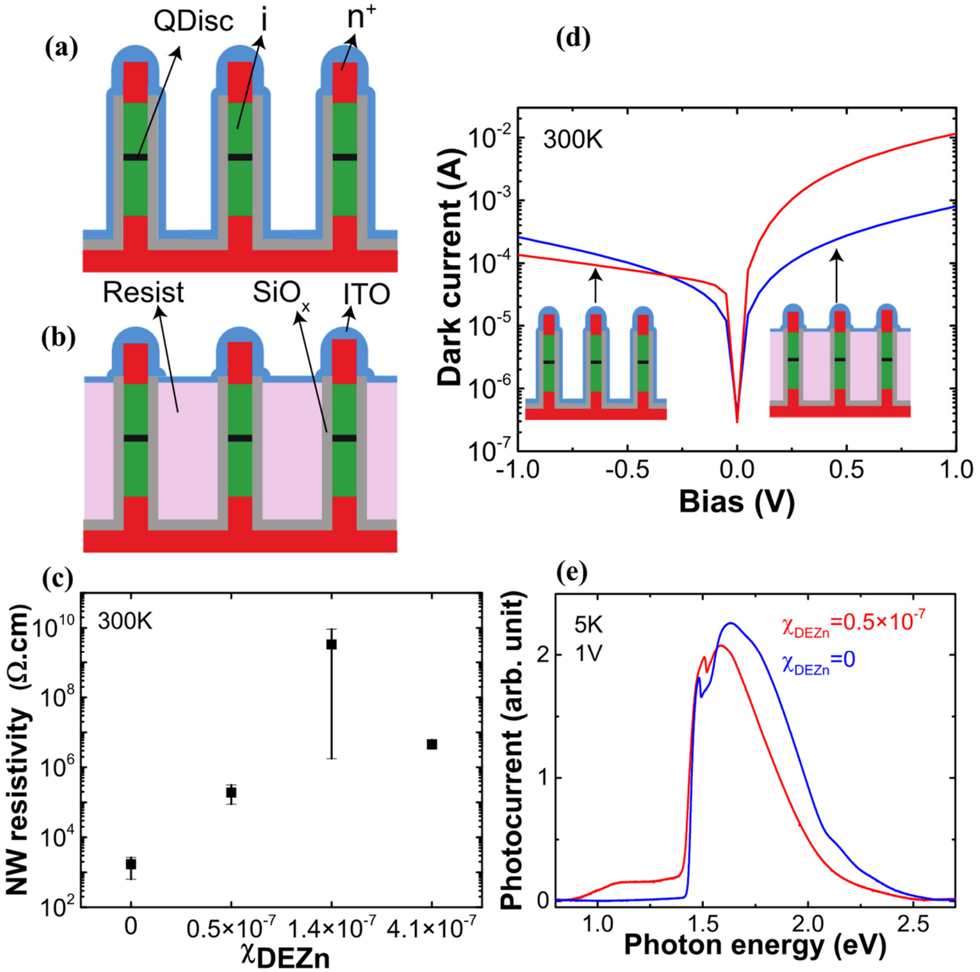

Figure 4.1 (a) First processing scheme with ITO uniformly deposited on the oxide-capped NWs. (b) Second processing scheme with ITO sputtered on top of the resist acting as a spacer layer to prevent side-gating effects. (c) Average NW resistivity, with estimated error bars, of samples grown with different DEZn molar fractions and processed according to (a). (d) I− V characteristics of two array detectors grown with chosen Zn compensation. Red and blue traces correspond to devices processed according to (a) and (b), respectively. (e) Spectrally resolved photocurrent for two detectors comprising a single QDisc in each NW, grown with chosen Zn compensation (red trace) and without Zn (blue trace), both processed according to (b).

The I-V characteristics for these detectors showed an asymmetric behavior. Asymmetric I-V characteristics have previously been reported in planar quantum well photodetectors and were attributed to different effects such as dopant segregation or growth-induced thickness modulation of the quantum well[85,86]. However, the asymmetry observed in our devices was on average significantly stronger than expected for any of the aforementioned effects. We interpreted this asymmetry as the result of self-gating induced by the ITO/SiO_x/NW wrap-gate geometry. As ITO covers the NWs uniformly during nanofabrication, as shown in Figure 4.1 a, any applied bias could effectively induce carrier depletion/accumulation in the NWs, which would change the spatial distribution of the carrier concentration and consequently the measured current. In order to verify this hypothesis, another single QDisc-in-NW sample from the same growth run with χDEZn = 0.5×10^{-7} was fabricated according to the modified scheme in Figure 4.1 b. The embedding of the NWs in a thick, hard-baked photoresist clearly mitigates any self-gating effects by allowing just the tips of the NWs to be in contact with the ITO. Evidently, the I-V characteristics of sample A was significantly more symmetric (blue trace in Figure 4.1 d) confirming a reduced accumulation (at positive bias) and depletion (at negative bias) of electrons in the NWs. A theoretical comparison of induced self-gating (accumulation of electrons) in a NW processed according to the two investigated schemes using the semiconductor module of COMSOL confirmed asymmetric characteristics for NWs processed according to the scheme with self-gating (Figure 4.1a). Spectrally resolved PC measurements were carried out on array detectors both with and without Zn compensation. Evidently, the interband PC signal from the InAsP QDiscs starting at 0.9 eV was much more prominent with added Zn (Figure 4.1 e) due to the dark current reduction and an enhanced collection of photogenerated carriers induced by a better optimized electric field distribution.

4.2 Current-voltage and photocurrent characterization

In order to increase the PC contribution from the InAsP QDiscs, we made a new series of samples with 20 QDiscs in each NW using the optimized growth parameters discussed above. An SEM image of the grown NW array is shown in Figure 4.2 a. Transmission electron microscopy (TEM) images showed that the grown QDiscs had thicknesses of 10 ± 1 nm. Energy dispersive X-ray spectroscopy (EDX) revealed fairly sharp InAsP/InP interface transitions (Figure 4.2 b). Point measurements of the composition in the QDiscs yielded As concentrations between 60 and 80%. PL measurements revealed a relatively broad peak between 0.9 and 1.2 eV at 5 K (Figure 4.2 c). The peak width most likely reflects the combination of variations in QDisc thickness and composition. A simple estimate of the wurtzite $InAs_xP_{1-x}$ bandgap would be 0.67−0.86 eV for $0.6 < x < 0.8$ (estimated from EDX) using an InAs and InP WZ bandgaps of 0.48 and 1.49 eV[87,88], respectively, and a bowing parameter of 0.1 eV[89] at 4 K. We attributed the observed blue-shift in PL compared to the estimated bandgap of the QDiscs to quantum confinement.

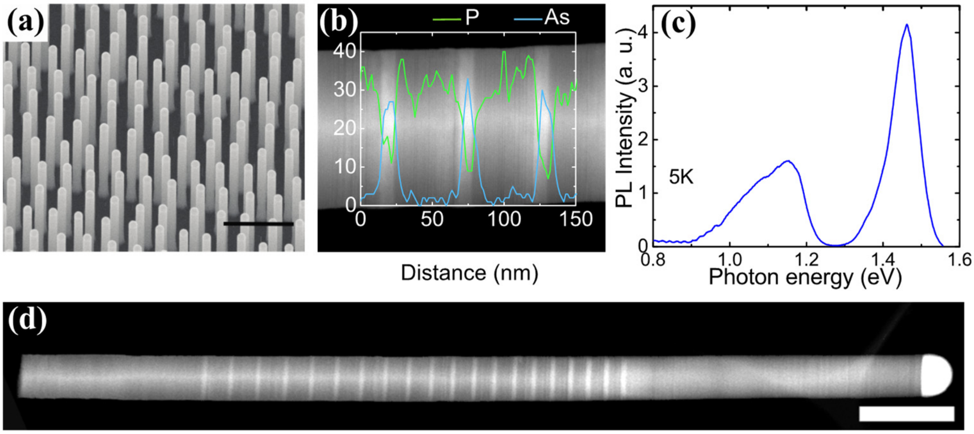

Figure 4.2 (a) SEM image of an as-grown InP n^+–i–n^+ NW array with 20 InAsP QDiscs in each NW. The scale bar is 1 µm. (b) EDX linescans overlaid on a TEM image of a NW. Green (blue) color represents P (As), respectively. (c) Typical PL and (d) TEM of a representative NW. The scale bar is 200 nm.

We fabricated two samples with 20 QDiscs, one without DEZn (sample B) and one with DEZn (sample C) to reduce the dark current. The samples where processed with photoresist infill to avoid any side-gating effects, as shown in Figure 4.3 a. The results from the I-V characterization presented in Figure 4.3 b shows a 4 orders of magnitude reduction in dark current from 300 K to 5 K at -2 V indicating efficient trapping of carriers at low temperatures in the staggered potential landscape introduced by the multiple QDiscs (sample B). I-V measurements on sample C showed a further four orders of magnitude reduction of dark current in a broad temperature range as compared to sample B confirming the successful compensation of residual n-doping in intrinsic region (Figure 4.3 c).

Figure 4.4 a, shows the spectrally resolved PC of samples B and C measured at 5 K. Clear spectral signatures of InP ZB and WZ crystal structures were visible in both samples. The PC with onset of about 0.75 eV is attributed to the QDiscs. The QDisc interband PC exhibits a broad signal with several peaks, which can be explained by thickness and compositional variations of the QDiscs, or by different electronic transitions in the QDiscs.

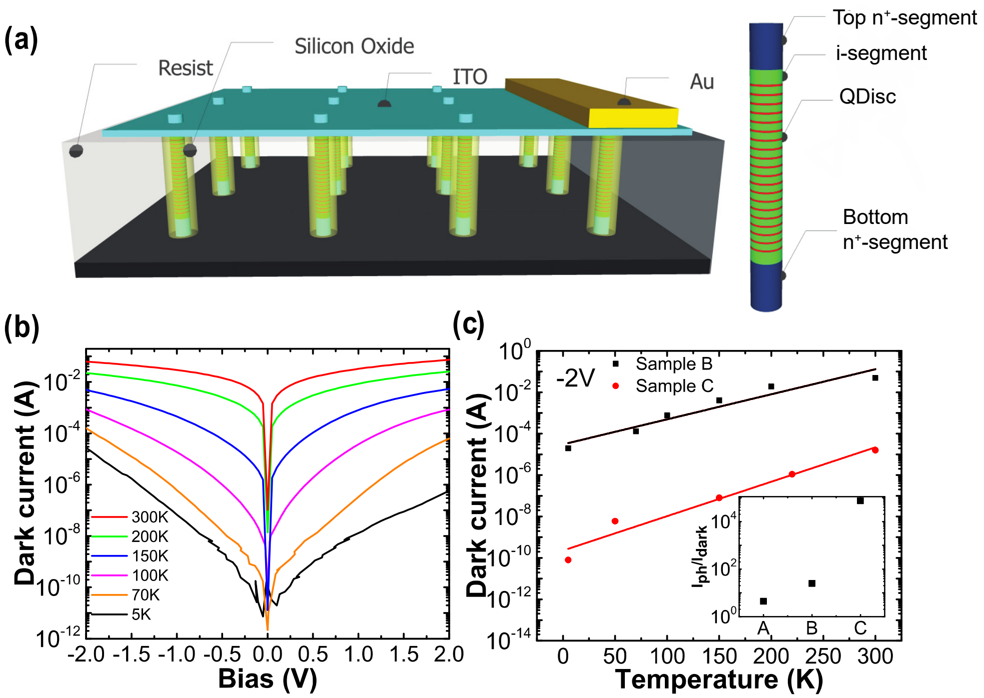

Figure 4.3 (a) Schematics of a vertically processed 20 QDiscs-in-NW array detectors. (b) Temperature dependence of the dark I-V characteristics of sample B (without Zn). (c) Comparison of the dark current at −2 V bias of samples B and C at different temperatures. The inset highlights the trend of increasing Iph/Idark by introducing multiple discs and adding Zn (T = 5 K).

A general observation is that the PC is strongly enhanced with increasing temperature. The onset of about 0.60 eV at 300 K is red-shifted compared to the 5 K onset by about 150 meV, which can be attributed to both the temperature-dependence of the bandgap (about 70 meV)[87,90] and to an enhanced thermal excitation of photogenerated carriers from the QDiscs to the InP NW matrix. Figure 4.4 c shows the spectrally resolved responsivity of sample C, extracted from the PC data in Figure 4.4 b using calibrated photodiodes. In order to cover the full spectral range of the NW detector, both Ge and Si photodiodes had to be used to extract the responsivity. Evidently, the relative contribution from the QDiscs, compared to the InP NW matrix, appears reduced compared to the PC presented in Figure 4b. This is due to a reduced transmission of the CaF_2 beam splitter, and a weakly reduced intensity from the quartz lamp, in the range 1.1–2.4 eV. It should be noted, however, that the responsivity in the spectral region covered by the QDiscs amounts to 0.6 A/W (at 0.9 eV), steadily increasing with applied bias to 7 A/W at 2 V bias (inset of Figure 4.4 c). This value is significantly higher than the typical responsivity of commercially available InGaAs, Ge, and Si photodiodes (the calibrated detectors used in this study both have a peak responsivity < 1 A/W).

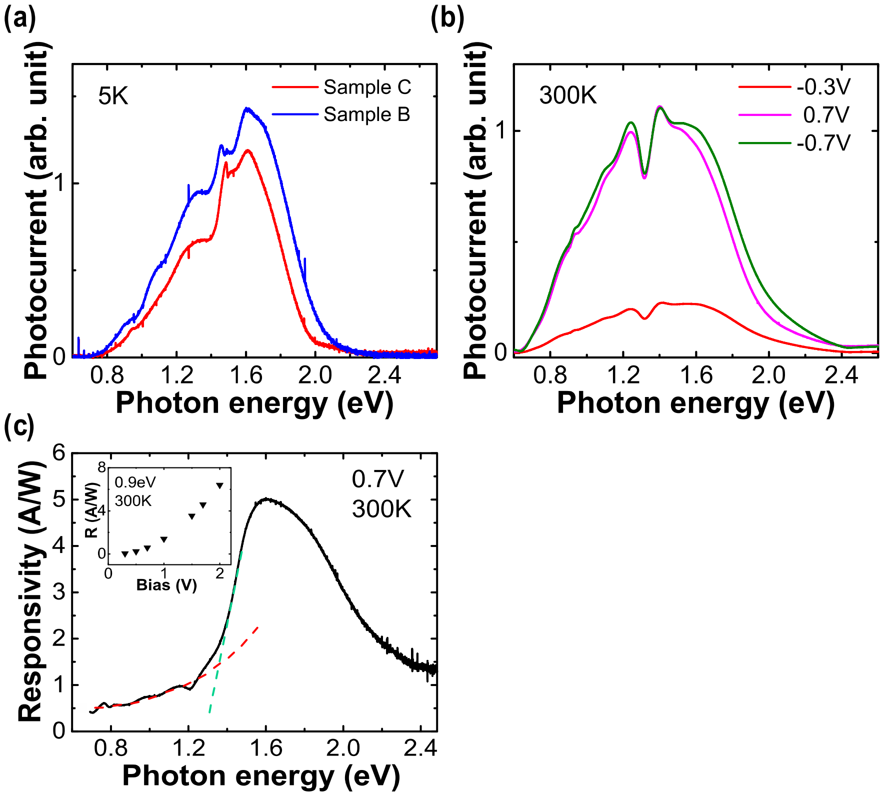

Figure 4.4 Spectrally resolved PC for (a) samples B and C at 5 K and −0.3 V applied bias and (b) sample C at 300 K for varying applied biases. (c) Spectrally resolved responsivity of sample C at 300 K and 0.7 V bias. The dashed colored lines are guides for the eye, indicating contributions from the QDiscs and InP NW, respectively. The inset shows the responsivity as a function of applied bias at 0.90 eV (1.38 μm).

This chapter was dedicated to InP NW array photoconductors, comprising single or 20 inserted InAsP QDiscs in each NW, grown by MOVPE demonstrating a detection range of up to 2 μm. It was shown that the dark current of the devices can be reduced by more than 4 orders of magnitude by adding Zn to compensate the unintentional n-doping in the intrinsic region. From spectrally resolved PC measurements it was concluded that the QDiscs provide a strong PC contribution with a bias-tunable responsivity reaching 7 A/W @1.38 μm at 2 V bias, and a significantly extended spectral sensitivity window to about 0.60 eV (2.0 μm) at room temperature. Also, we investigated the effect of radial depletion, due to an effective wrap-gate design, induced by covering the sides of the NWs by ITO and SiO_x during processing of the detectors.

5 High responsivity of InP nanowire arrays photodetectors with embedded quantum heterostructures

In this chapter we discuss the responsivity of InP NW arrays with embedded InAsP quantum discs under illumination with a broadband quartz lamp source, a 532 nm laser, and a 980 nm laser, for various intensities and modulation frequencies. The measurements demonstrate a remarkable responsivity of the fabricated photodetectors as high as 250 A/W at 980 nm/ 20 nW and 990 A/W at 532 nm/60 nW, both at 3.5 V bias, far beyond the classical limit for photoconductive detectors. This indicates the presence of a novel photoconductive gain mechanism. To unravel the origin of the enhanced responsivity we performed full optoelectronic simulations using the commercial device simulator *Synopsys Sentaurus*, which solves the electron and hole continuity equations, including drift-diffusion currents, together with the Poisson equation. The simulation results revealed a lowering of the potential barrier between the highly doped n-region and the middle intrinsic region, induced by recombination of trapped electrons in surface traps and QDiscs with photogenerated holes. The simulated I-V behavior was in remarkably good agreement with the experimentally measured data.

5.1 Growth, fabrication and FTIR characterization

We followed the same procedures as discussed in Chapters 4 and 5 to grow the NWs using MOVPE. First, Au particles were patterned by nanoimprint lithography, metal evaporation, and lift-off. The growth was then carried out in a low-pressure (100 mbar) Aixtron 200/4 MOVPE reactor at 440 °C. The grown NWs have a diameter of 130 nm and a length of about 2 µm, with a designed n^+-i-n^+ doping profile. Tetraethyltin (TESn) was used as the doping precursor for the n-region and diethylzinc (DEZn) was used to compensate the residual n-doping in the intrinsic region. Also, the condition of the reactor was optimized to adjust the flow of DEZn as low as possible, to avoid any over-compensation that potentially can turn the doping profile to n^+-p^--n^+. The growth conditions for the InAsP QDiscs were the same as discussed in Chapters 4 and 5. The grown QDiscs had thicknesses of 8 ± 1 nm and an As concentration of 40% ± 10% as observed by multiple point TEM/EDS analysis and full quantifications. Figure 5.1 (a) and (b) show TEM images and overlaid EDS spectra of As and P, respectively.

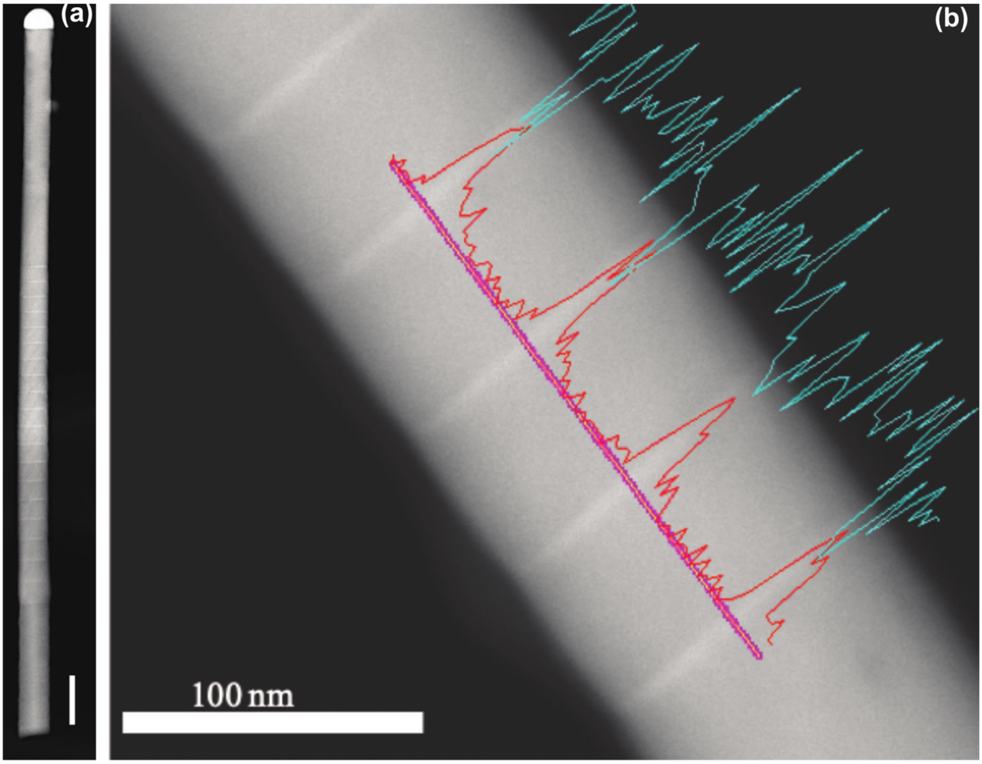

Figure 5.1 (a) TEM image of a single NW revealing the 20 axial $InAs_{0.40}P_{0.60}$ QDiscs (scale bar is 200 nm). (b) The overlaid EDS spectra show the presence of As (red trace) and P (cyan trace). Point analysis and quantification in the center of the discs confirm an As composition of 40% ±10%.

The vertical processing of the device is also optimized to achieve the highest performance level. After encapsulating the NWs by SiO_x and back etching of the photoresist to expose the tips of the NWs, we noticed a discontinuity between the infill photoresist and oxide layer, possibly occurring due to lateral etching of the oxide by BOE. This discontinuity can lead to a poor top contact layer by not allowing ITO to uniformly deposit through the device. Hence, we removed the photoresist after exposing the tips and respun a second round of photoresist, followed by back etching to avoid the discontinuity. Figure 5.2 shows different steps of the processing of the fabricated device.

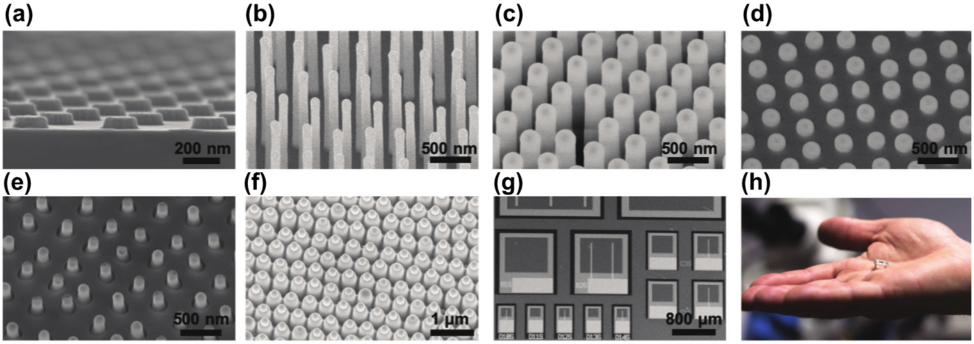

Figure 5.2 Fabrication steps to realize the present NW array photoconductors. (a) Definition of Au seed particles by NIL. (b) Growth of InP/InAsP NWs using MOVPE. (c) Capping of the grown NWs by a SiO_x layer using atomic layer deposition (ALD). (d) Embedding of the NWs in a thick photoresist (S1818) layer and subsequent back-etching to expose 300 nm of the NW tips. (e) Etching of SiO_x and Au particles from the tips. (f) Sputtering of 50 nm ITO on top of the NWs as a transparent contact. (g) Definition of device areas using UV lithography, followed by deposition of 400 nm thick gold bond pads. (h) Sample mounted on a DIL holder and bonded for optoelectronic characterization.

The optoelectronic characterization started by measuring the I-V traces of the device under dark and broadband (quartz lamp) illumination conditions as shown in Figure 5.3 (a). The device shows the expected antisymmetric I-V behavior of a successfully realized n^+-i-n^+ structure. The dark current at -1 V amounts to about 35 pA/NW at 300 K, proving a successful suppression of the dark current by compensating residual n-dopants in the intrinsic region. The extracted PC of the device, obtained by subtracting the dark current from the total current under illumination, is shown in Figure 5.3 (b). Fourier transform infrared (FTIR) spectroscopy was carried out to investigate the spectral distribution of the PC. The measured PC data were subsequently converted to responsivity using two NIST-calibrated Ge and Si photodiodes from Thorlabs. The spectrometer (Bruker Vertex 80 V) was equipped with a quartz lamp, with an intensity of about 10–15 mW/cm^2 (at the sample position) in the spectral range 500–1100 nm, and a CaF_2 beam splitter. The spectrally resolved responsivity from 0.70 eV to 1.35 eV in Figure 5.3 (c) is attributed to interband transitions between the electron and hole ground states in the $InAs_{0.40}P_{0.60}$ QDiscs. The presence of several peaks in the range 0.7–1.35 eV can be attributed to different electronic transitions between confined energy levels in the QDiscs, as well as to variations in QDisc thickness and As composition. The sharp increase in responsivity at about 1.35 eV reflects the onset of interband excitation of the InP NWs. The responsivity increases strongly with applied bias, as expected from the strongly bias-dependent PC in Figure 5.3 (b), reaching a peak responsivity of 16 A/W at a bias of 2 V. Figure 5.3 (c) also shows the gain at 2V calculated from the responsivity. Here, it should be noted that the measured data in Figure 5.3 (a) and (b) are taken under DC conditions, while the illumination during the FTIR measurements is modulated by the scanning mirror at a frequency of about 7.5 kHz.

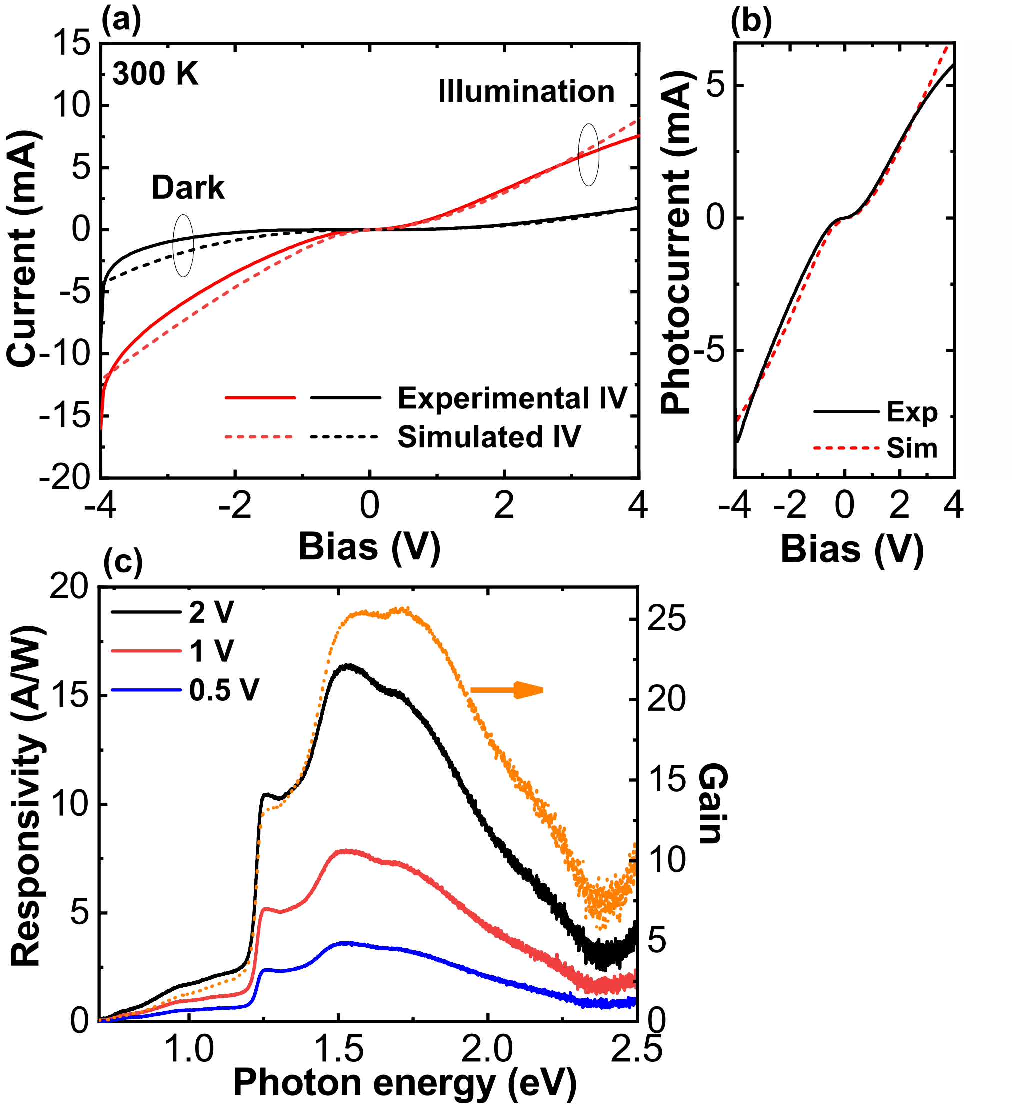

Figure 5.3 Typical optoelectronic characteristics of a fabricated NW photoconductor at 300 K. (a) I-V in the dark (black traces) and under illumination (red traces). The solid lines are experimental data while the dashed lines are simulations. (b) Photocurrent obtained by subtracting the dark current from the total current under illumination. (c) Spectrally resolved responsivity versus photon energy at three different biases (solid lines, left axis) and calculated gain at 2 V (dotted line, right axis)

5.2 Optoelectronic modeling of gain mechanism

The observed PC and responsivity data are, to the best of our knowledge, higher than any other reported values for III-V NW-based photodetectors in the same wavelength region. Seyedi et al. reported on GaAs/AlGaAs core-shell NWs grown on a GaAs substrate with a responsivity reaching 0.65 A/W at 300 K and 850 nm wavelength[91]. Lee et al. reported on InAsSb NWs grown on a GaAs substrate with a responsivity of 0.194 A/W in the range of 1000–3500 nm[92]. The only report of InP NW arrays with embedded quantum heterostructures photodetectors outside our group is by Kuyanov et al. where they synthesized InP NWs with axial InAsP quantum dots on a silicon substrate[76]. For their devices, however, only 17% of the NWs were standing vertically, and the devices demonstrated a low photosensitivity. In order to unravel the detailed underlying mechanism behind the large observed PC in our detectors, we have carried out extensive modeling of our NW detector arrays including traps located at the interface between the NW and SiO_x shell. The simulations were carried out with the commercial device simulator *Synopsys Sentaurus* which solves the electron and hole continuity equations, including drift-diffusion currents, together with the Poisson equation. A high gain in photoconductors is often understood in terms of the well-known photon-recycling model in which the optical gain, i.e., the ratio of the number of photogenerated charge carriers to the number of absorbed photons, is proportional to the ratio between minority carrier lifetime and corresponding transit time across the photoconductor. This explanation, however, assumes that the distribution of photogenerated carriers is uniform across the photoconductor, an assumption that is unrealistic due to the presence of metallic contacts to the detector and the high applied electric field induced by the applied bias. Dan *et al.* have shown that the gain in photoconductors can in fact only exceed unity if there is a large imbalance in the ratio of majority to minority photocarrier density, or in the ratio of majority to minority carrier mobility[93]. However, their explanation disregards the effect of a feedback mechanism involving trapped charge carriers in the electrostatic potential. We have developed a novel model that describes the complex dynamics involved in carrier trapping and recombination in the embedded QDiscs and interface traps in darkness and under illumination in great detail. For the modeling, we have used an accurate 2D geometrical model of the NWs directly extracted from a TEM image, with rotational symmetry around the central axis, including the QDiscs with correct thickness and accounting for the variation in spacing between the discs. The schematic of the simulated structure is shown in Figure 5.4 (a). Also, interface recombination is included by adding shallow acceptor traps at the NW/SiO_x interface, with an energy of 100 meV below the conduction band edge of both InP and $InAs_{0.40}P_{0.60}$. A trap density of 9×10^{11} cm^{-2} and a capture cross section of 1.5×10^{-20} cm^2 were chosen from a fitting to the experimental data. The dashed lines in Figure 5.3 (a) and (b) are simulated I-V characteristics of a complete NW array detector element. Evidently, the measured and simulated I-V characteristics in dark and under illumination are in excellent agreement. Figure 5.4 (b) shows the calculated room-temperature band diagram along the center of a NW at an applied bias of 1 V. The intrinsic region creates an electrostatic barrier for the electrons, which leads to a resistive behavior. In addition, electrons are trapped in the dark by the QDiscs and acceptor-like states present at the NW/SiO_x interface. This negative immobile charge effectively leads to a radial depletion of the intrinsic region due to electrostatic forces, further reducing the electron density by 2 orders of magnitude. The radial depletion also leads to a radial dependence of the band diagram, where the conduction band bends up toward the surface of the NWs. The resulting electrostatic potential creates a significantly higher barrier for the majority electron current, in effect similar to a negatively charged gate in a field-effect transistor. Under illumination, electron-hole pairs are generated in the NW. The minority holes can efficiently recombine with the trapped interface electrons, reducing the trap occupation substantially. In Figure 5.4 (b) this is shown on the right-hand axis, where the trap occupation probability is plotted (1 is equivalent to 100% trapping probability). Lowering the local density of immobile electrons leads to a lowering of the electron barrier for electrons, and thereby to a substantial increase in the current through the wire and a responsivity much higher than the classical limit as discussed above.

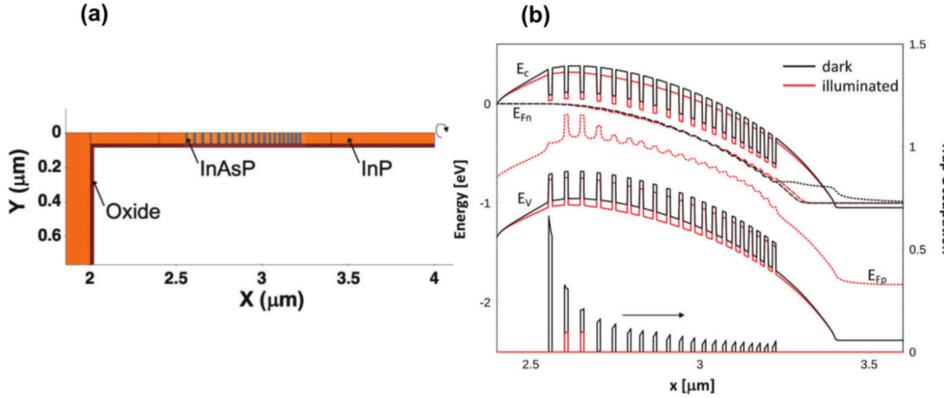

Figure 5.4 (a) Geometry of the simulated NW structure, with a rotational symmetry axis around y = 0. The position and thickness of the individual QDiscs along the NW are taken from a TEM image. (b) Upper panel shows the schematic band diagram of the intrinsic region along the center of the NWs with embedded QDiscs at an applied voltage of V = 1 V in the dark (black lines) and under illumination (red lines). The corresponding quasi-Fermi levels are also displayed and marked by E_{Fn} and E_{Fp}, respectively. The lower panel shows the electron occupation probability (right-hand side scale) in the proposed interface traps of the NWs in the dark and under illumination. T = 300 K.

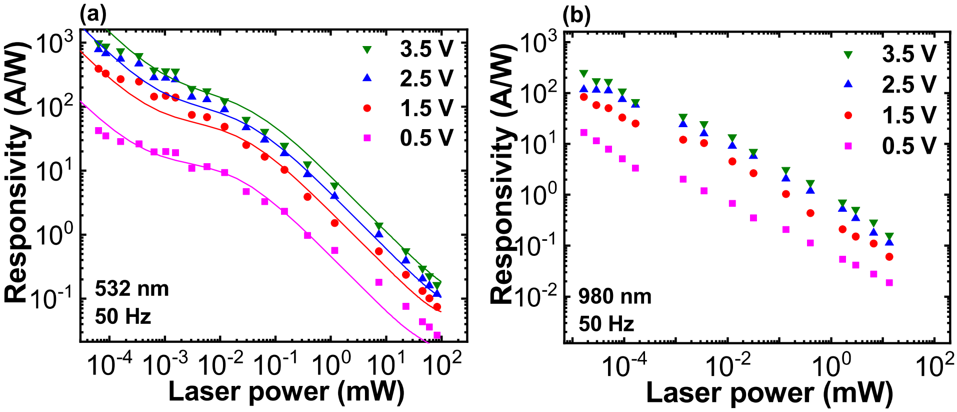

Figure 5.5 (a) Responsivity versus laser power and applied bias at 532 nm laser wavelength. The symbols are experimental data, while the solid lines are derived from the modeling. (b) Responsivity versus laser power and applied bias at 980 nm laser wavelength. All experimental PC values are taken using a standard lock-in technique at f = 50 Hz.

5.3 Responsivity for different laser wavelengths and intensities

The extracted responsivity for 532 nm laser illumination for different applied biases is shown in Figure 5.5 (a). The highest responsivity at a 50 Hz chopper frequency amounts to 990 A/W for an optical power of 60 nW and a bias of 3.5 V. The responsivity strongly reduces with increasing laser power as expected from the proposed photogating effect involving traps. The illumination leads to a lowering of the electron barrier due to recombination of interface-trapped electrons with photogenerated holes. However, high optical generation levels lead to interface electron densities lower than or equal to the surrounding majority electron density, and hence to a saturation of the PC and a drop-in responsivity. The dashed lines in Figure 5.5 (a) are the calculated responsivity values, which evidently are in very good agreement with the experimental data. Moreover, we also performed a simulation without including interface traps, thus removing the strong photogating effect, which resulted in responsivity values that were within the standard theoretical limit for photoconductors. This result confirms that interface traps are necessary in order to explain the experimental data. The NW photoconductors also demonstrated a high responsivity for 980 nm laser illumination as shown in Figure 5.5 (b). The highest responsivity at 50 Hz chopper frequency obtained for this laser wavelength was about 250 A/W for an optical power of 20 nW and a bias of 3.5 V. We note that the maximum responsivity values at 532 and 980 nm recorded at 50 Hz are much higher than those shown in the spectrally resolved data in Figure 5.3

(c). There are two reasons for this difference: (i) the intensity of the quartz lamp used in the FTIR setup is much higher than 60 nW, which leads to a lower responsivity from the discussion above, and (ii) the modulation frequency of the light in the FTIR (~7.5 kHz) is much higher than the chopper frequency of 50 Hz used in the lock-in laser setup. A higher modulation frequency reduces the PC significantly. The highest responsivity is thus obtained for a low modulation frequency combined with a low light intensity. The extracted specific detectivity of $D^* = 2 \times 10^{10}$ $(\text{cm}^2\ \text{Hz})^{1/2}/\text{W}$ was obtained at a bias of 0.5 V and 532 nm.

Table 5.1 Comparison of different reported NW-based infrared photodetectors

Material	**Sub strate**	**Area (mm^2)**	**T (K)**	**λ (μm)**	**R (A/W)**	**Gain**	**D^* (Jones)**	**Dark current**	**Ref**
InAs	InP	0.01	RT	1.2 – 2.5	1.25×10^{-3}	0.08×10^{-3}	2.5×10^{7}	130 mA/cm^2 @ 0.5V	[94]
InAs	Si	4	77	1.4 – 3.3	60.45×10^{-3}	9.2×10^{-2}	1.9×10^{8}	0.5×10^{-4} mA/cm^2@ 0.05 V	[75]
InP/InAsP QDs	Si	2.4	RT	0.8 – 1.4	NA	NA	NA	0.2nA @ -1V	[76]
GaAsSb	Si	50	RT	0.633 – 1.1	311	NA	1.9×10^{10}	NA	[95]
InAsSb	GaAs	0.0025	77 – 220	1 – 3	0.194	NA	NA	200 mA/cm^2 @ 0.1V	[92]
InAsSb	InAs	NA	5	3 – 5.7	NA	NA	NA	3×10^{-3} mA @ 0.1V	[96]
GaAs/AlGaAs	GaAs	0.01	RT	0.85	0.65	NA	NA	100 μA/cm^2 @ -2V	[91]
InP/InAsP	InP	0.64	RT	0.5 – 2	7	NA	NA	20 μA @ -2V	[97]
InP/InAsP	InP	0.64	RT	0.5 – 1.7	250 @ 980 nm 990 @ 532 nm	25	2×10^{10}	100 μA @ -1V	This work

In Table 5.1, we summarize the characteristics of NW-based IR detectors reported in literature, and compare those to the results presented in this chapter. Finally, we also investigated the time response of the photodetectors at 532 nm using a chopper at 1 kHz (100 rev./s) combined with a storage oscilloscope. From the PC trace shown in Figure 5.6 we extract a rise time and decay time of 33 and 207 μs, respectively. The rise time is limited by the tangential velocity at the rim of the chopper wheel. The much longer decay time reflects a persistent photoconductivity effect, attributed to radial band bending which leads to a spatial separation of photogenerated electrons in the NWs and holes captured by the interface traps. The obtained rise and decay times are comparable to those recently reported for NW-based photodetectors, demonstrating the potential of the present NW array photodetectors[98].

In conclusion, in this chapter we comprehensively studied the responsivity of broadband n^+-i-n^+ nanowire array photoconductors with embedded quantum heterostructures. The photodetector demonstrated a broadband photoresponse and an ultrahigh responsivity and gain that depends on both the applied bias and the optical power. Advanced modeling, based on realistic nanowire structures, revealed that the high responsivity can be explained by a photogating feedback mechanism on the electrostatic band profile. This feedback mechanism, originating from the complex charge carrier dynamics involving interface traps and the quantum discs, reduces the electron transport barrier between the highly doped n$^+$ contact and the i-segment under illumination.

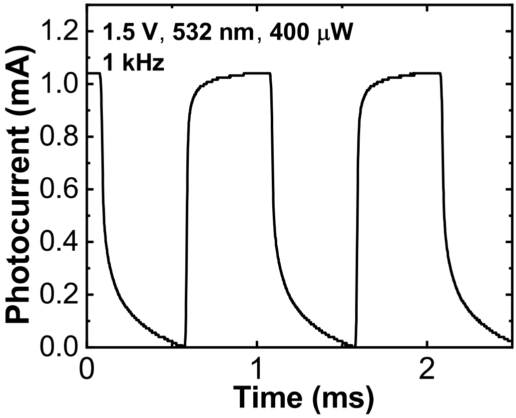

Figure 5.6 Oscilloscope trace of the recorded PC at 1 kHz chopper frequency. A residual persistent photoconductivity effect is evident from the fairly slow recovery transient.

6 Intersubband InAsP/InP quantum discs-in-nanowire photodetectors

Although there has been a great effort in developing high performance photodetectors based on NWs, the operation wavelength is limited mostly to the NIR and SWIR regions. Svensson *et al*. reported on a NW-based photodetector in a low-bandgap InAs/InAsSb NW array that had a photoresponse peak at 4 μm with a long wavelength cut-off at approximately 5.7 μm.[9] Also, Zhou et al. reported on single crystalline SmB_6 NWs with a broadband photodetection range from 488 nm to 10.6 μm[99]. Intersubband transitions are an effective way to detect long wavelength photons because the energy separation between the corresponding electronic states can readily be tuned by the dimensions of the QWs/ QDs and their compositions. To the best of our knowledge, there are no previous reports on spectrally-resolved PC generation in a NW geometry for LWIR detection. In this chapter, we investigate intersubband transitions between confined energy levels in InAsP QDiscs embedded axially in InP NWs and capable of broadband detection at normal incidence in both the MWIR and LWIR ranges, extending to wavelengths as long as 20 μm. Also, we show that NWs host longitudinal modes which enables new opportunities for controlling and manipulating long-wavelength radiation in detecting and energy-harvesting devices.

6.1 Current-voltage and photocurrent characterization

Figure 6.1 shows SEM and TEM images along with EDX data of as-grown InP NWs comprising a single embedded InAsP QDisc. Complete photodetector elements were fabricated from these NW arrays using the processing scheme discussed in Chapter 3 with photoresist in-fill to mitigate self-gating effects. The low dark current levels demonstrated in Figure 6.2 a, falling by about 5 orders of magnitude from 1.6×10^{-3} A at 250 K to 1×10^{-8} A at 10 K at a bias of 0.5 V, exhibit symmetric voltage dependence. Spectrally resolved PC shows that the fully processed device exhibits a broad spectral response across the visible and NIR regions from 0.9–2.4 eV (0.5–1.4 μm) at room-temperature.

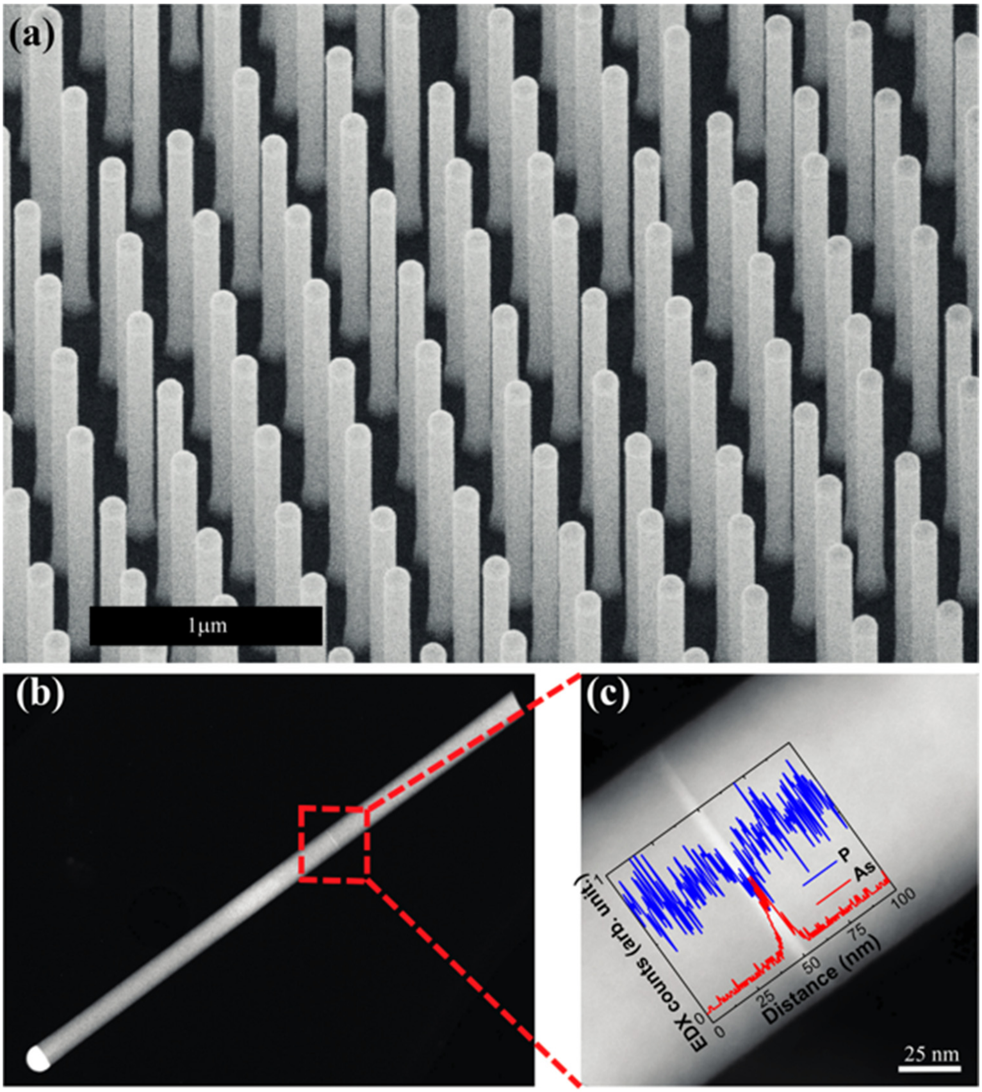

Figure 6.1 (a) SEM image of an as-grown InP NW array with a single embedded InAsP QDisc in each NW. (b) Low-resolution STEM image of a NW with an embedded disc. (c) A higher-resolution image showing the QDisc, overlaid with an EDX linescan. The EDX profile show that the discs are not abrupt and have an average thickness of 7−8 nm.

We attribute the PC response in the 1.3−2.4 eV range to interband transitions in the InP and in the 0.9−1.3 eV range to interband transitions between confined energy levels in the InAsP QDisc (Figure 6.2 b). The semi-log plot of the PC in Figure 6.2 d clearly indicates two interband transitions with onsets of about 0.95−1.0 eV and 1.1−1.15 eV, respectively. The inset in Figure 6.2 d shows the assignment of the corresponding underlying optical transitions in the QDiscs. The proposed smooth and asymmetric confinement potential is inferred from the EDX data in Figure 6.1 c. Strong peaks in the energy range between 1.45 and 1.65 eV are interpreted as interband transitions in the zincblende (ZB) and wurtzite (WZ) segments of the polytype InP NWs. The temperature-dependent PC spectra in Figure 6.2 c show a strongly reduced trapping of electrons at elevated temperatures by the staggered conduction band landscape induced by the embedded QDiscs and the polytype ZB/WZ InP crystal structure.

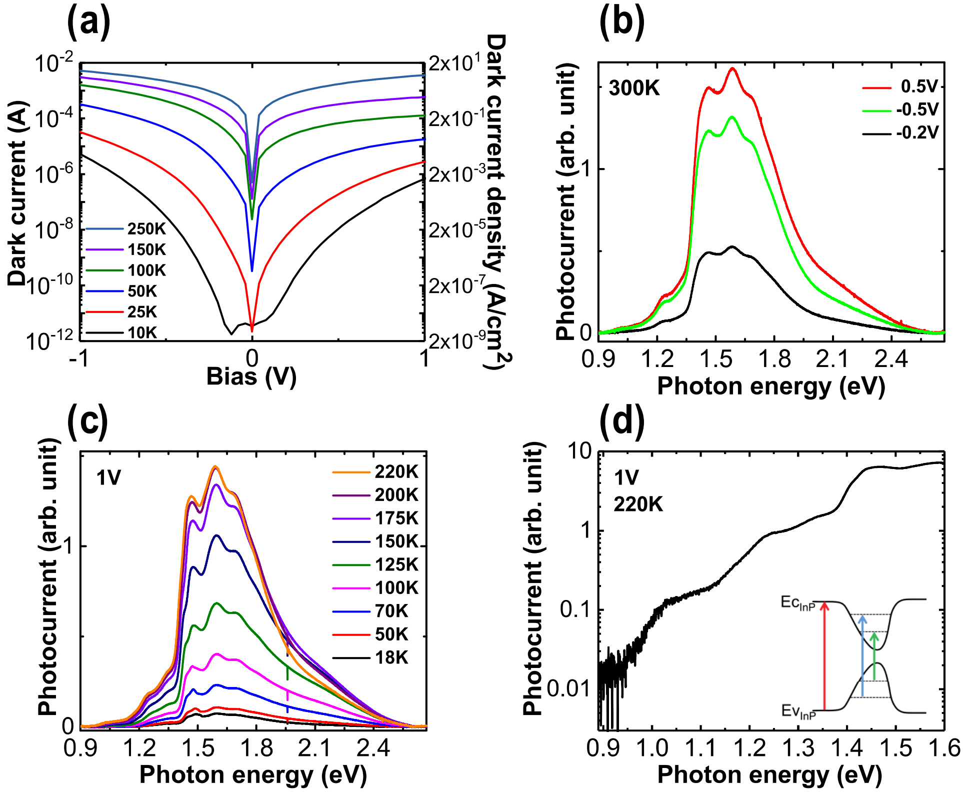

Figure 6.2 I-V characteristics and spectrally resolved interband PC of a single-QDisc-in-NW photodetector. (a) I-V characteristics in darkness measured at different temperatures. (b) PC at 300 K for different applied biases. (c) PC at 1 V bias vs temperature and (d) PC at 220 K, taken from panel c, in a semi-log scale. Inset shows schematically the relevant interband transitions in the QDisc.

At low temperatures, spectrally resolved PC spectra show that the devices exhibit a PC response that extends out to approximately 20 µm. The PC spectrum of the single-QDisc-in-NW detector (Figure 6.3 a) shows a large PC signal centered around 0.1 eV at normal incidence, having an apparent double-peaked structure with peaks at approximately 0.08 and 0.12 eV. Additionally, two smaller photocurrent peaks are observed at 0.20 and 0.40 eV. These PC signals in the MWIR and LWIR regions were recorded after switching from interband (CaF_2 beam splitter and quartz lamp) to intersubband (KBr beam splitter and globar filament source) spectrometer settings. We observe that the intensity of the intersubband PC signal is largest at normal incidence and is reduced as the angle of incidence increases (Figure 6.3 b). This behavior is in sharp contrast to conventional planar QW detectors that exhibit very small PC signals at normal incidence because of the fundamental selection rules for intersubband transitions.

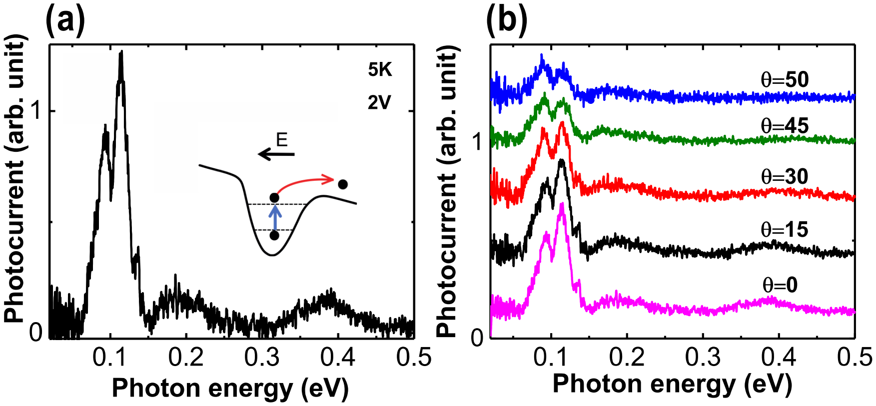

Figure 6.3 (a) Spectrally-resolved intersubband PC at normal incidence excitation. The inset shows schematically the electronic structure of the discs with indicated energy levels and the main optical intersubband transition (blue arrow) behind the experimentally observed signal at about 0.1 eV. (b) PC spectra taken at various angles of incidence relative to the normal of the sample.

The electronic origin of the intersubband transitions in our single-QDisc-in-NW detector can qualitatively be understood from calculations of the band structure of the InAsP QDiscs using an 8-band $\mathbf{k} \cdot \mathbf{p}$ model[89] which shows the existence of two states inside the conduction band of the $InAs_{0.55}P_{0.45}$ QDiscs: a ground state at 0.22 eV and an excited state 0.05 eV below the conduction band of the InP. As mentioned above, the As composition varies significantly across the thickness of the QDiscs which leads to a smoothed potential profile. In effect, this pushes up the ground state and lowers the excited state of the QDisc compared to a hard-wall QW potential. Based on these arguments, the double-peak structure centered around 0.1 eV can be attributed to an intersubband transition between the QDisc's ground state and excited state, followed by a subsequent escape to the InP NW continuum. The dip at 0.1 eV (12.4 μm) between the peaks at 0.08 and 0.12 eV is attributed to strong optical phonon absorption[100] induced by SiO_2 shell around the NWs, which decreases the amount of light that reaches the QDisc.

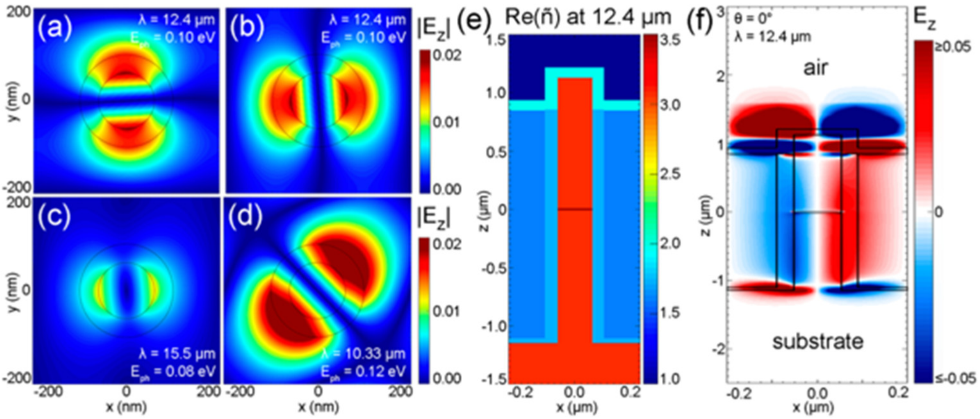

Figure 6.4 2D FDE model, 3D FDTD model, and the results of EM modeling. (a,b) Amplitudes of the longitudinal component, $|E_Z|$, of the first and second mode at λ = 12.4 μm, respectively. (c,d) Amplitudes of the longitudinal component, $|E_Z|$, of the first mode at λ = 15.5 μm and of the second mode at λ = 10.33 μm, respectively. In panels a−d, the edges of the InP and SiO2 regions are indicated by black lines. (e) 2D cross-section of the 3D unit cell in the x-z plane showing the real part of the complex refractive index at λ = 12.4 μm. Colors indicate the InP substrate and wire (red), the QDisc (dark red), the oxide (light blue), the photoresist (dark blue), the ITO (aqua), and air (dark purple). (f) A slice in the x-z plane of the 3D FDTD model of the longitudinal component, E_Z, of the electric field for λ = 12.4 μm at normal incidence (θ = 0).

6.2 Optical simulation results

Optical modeling of a complete single-QDisc-in-NW detector shows a photonic crystal behavior of the device that hosts very different optical modes compared to conventional planar QWIPs. According to eigenmode solutions to Maxwell's equations on a 2D cross-section, the device supports two optical modes in the 3−20 μm wavelength range having nonzero longitudinal E_Z components for normally incident optical excitation that extend from the low-index dielectric matrix into the high-index NW (Figure 6.4 a−d). These modes ensure that even at normal incidence, the E_Z component of the electric field necessary to excite intersubband transitions in the QDiscs is present within the NWs. The variation in longitudinal component amplitude indicates that the intersubband absorption strength may vary with wavelength. For example, the FDE model shows that the longitudinal component amplitude at 10.3 μm (0.12 eV) is significantly greater than at 15.5 μm (0.08 eV) (Figure 6.4 c,d), in agreement with our experimental observation that the PC signal is significantly stronger at 0.12 eV than at 0.08 eV at normal incidence (Figure 6.3 a). A slice of the E_Z component of the electric field for a wavelength of 12.4 μm at normal incidence (Figure 6.4 f) shows that the wave acquires an E_Z component that extends into the NW as it passes through the nanostructured layer of the device and that this E_Z component vanishes as the wave passes into the substrate. The presence of a finite E_Z component induced by the nanostructured parts of a photonic crystal partly explains the intriguing existence of a normal incidence signal in our NW array detectors. An additional effect that influences the sensitivity to normal incidence radiation is the compositional variation along the discs (as extracted from the EDX data in Figure 6.1 c). This creates a smooth, asymmetric potential that lacks inversion symmetry (as indicated in the inset of Figure 6.3 a). This compositional variation most likely reflects As carryover[101,102] which leads to a significantly sharper transition from InP to InAsP than that from InAsP to InP. Moreover, our QDiscs are grown using the deplete growth which might induce further compositional changes compared to conventional planar growth. The absence of inversion symmetry in the confining potential washes out the definite parity of the corresponding wave functions and leads to nonvanishing oscillator strength in the intersubband transitions at normal incidence.

In conclusion, in this chapter we discussed detection of long-wavelength infrared absorption in NWs and PC originating from intersubband transitions in NW heterostructures. We realized photodetectors that exhibit a photoresponse from the visible to the far-infrared. Additionally, we observe PC caused by intersubband transitions under normal incidence illumination, which is attributed to a photonic crystal behavior of NWs having nonzero longitudinal components that extend out of the low-index dielectric matrix and into the high-index NWs.

7 Summary and Outlook

In this thesis work, we have demonstrated the successful development of novel NW-based broadband photodetectors. We showed that unintentional doping in NWs can increase the dark current leading to poor detector performance. To eliminate this effect, we introduced Zn as compensatory in-situ doping. I-V characterization showed that the dark current reduced by about 4 orders of magnitude in a broad temperature range. Also, we observed a self-gating effect arising from the radial NW/SiO_x/ITO design leading to an asymmetric I-V behavior. Filling the space between the NWs by a photoresist avoids the formation of this side-gating effect and symmetrizes the I-V characteristics of the detectors. A room-temperature responsivity of about 7 A/W @1.4 µm for 2 V bias was reported for InP NW array detectors with 20 InAsP quantum discs embedded in each NW. We also performed an in-depth experimental and theoretical investigation of the responsivity of optimized photodetectors under different illumination conditions. The photodetectors exhibit strongly bias and power-dependent responsivities reaching record-high values of 250 A/W at 980 nm/20 nW and 990 A/W at 532 nm/60 nW, both at 3.5 V bias. Complementary real device modeling revealed a new photogating mechanism, induced by the complex charge carrier dynamics involving optical excitation and recombination in the quantum discs and interface traps, which reduces the electron transport barrier between the n^+ segment and the i-segment under illumination.

We have also demonstrated the first NW array intersubband photodetector with a photoresponse extending up to 20 µm with normal incidence sensitivity. FDTD simulations showed that the unexpected normal incidence response partly stems from photonic crystal properties of the NW array matrix which hosts non-zero longitudinal modes with an E_z component along the NWs.

Although we have been successful in fabricating state-of-the-art IR photodetectors using NWs, there are challenges remained to be solved. The demonstrated intersubband NW photodetectors are working only at very low temperatures around 5 K, which is far below the operation temperature of commercially available LWIR photodetectors. One reason is that the magnitude of the E_z component inside the NWs is very small. A solution to increase E_z is to embed the NWs in a photonic crystal, formed by a periodic pattern of dielectric materials such as SiO_x or AlO_x, that enhances E_z. Initial simulation results show that by proper designing of such a pattern, Ez can increase by three orders of magnitude inside the NWs.

Also, the mentioned side-gating effect in fact offers a new possibility to make three-terminal NW IR photodetectors for voltage-tunable broadband photoresponse. Applying a bias to the NW/SiO_x/ITO wrap-gate facilities a Fermi level (electron concentration) tuning inside the NWs and discs, which in turn provides not only a handle for controlling the dark current, but also to toggle between interband and intersubband functionality.

Our results show that the incorporation of heterostructures in NWs pave the way toward realizing disruptive high-performance photodetectors and image sensors capable of broadband detection resulting from interband and intersubband transitions.

8 References

1 Goldberger, J., Hochbaum, A. I., Fan, R. & Yang, P. Silicon vertically integrated nanowire field effect transistors. *Nano Letters* **6**, 973-977 (2006).

2 Wallentin, J. *et al.* InP Nanowire Array Solar Cells Achieving 13.8% Efficiency by Exceeding the Ray Optics Limit. *Science* **339**, 1057-1060 (2013).

3 Kim, S.-K. *et al.* Doubling absorption in nanowire solar cells with dielectric shell optical antennas. *Nano Letters* **15**, 753-758 (2014).

4 Q Peng, K., P Huang, Z. & Zhu, J. Fabrication of large-area silicon nanowire p–n junction diode arrays. *Advanced Materials* **16**, 73-76 (2004).

5 Berg, A. *et al.* Radial Nanowire Light-Emitting Diodes in the (Al x Ga1–x) y In1–y P Material System. *Nano Letters* **16**, 656-662 (2015).

6 Yan, L. *et al.* Structural and optical properties of disc-in-wire InGaN/GaN LEDs. *Nano Letters* **15**, 1535-1539 (2015).

7 Zeng, L. H. *et al.* High-responsivity UV-Vis Photodetector Based on Transferable WS2 Film Deposited by Magnetron Sputtering. *Scientific Reports* **6**, 20343 (2016).

8 Zhu, H. *et al.* Lead halide perovskite nanowire lasers with low lasing thresholds and high quality factors. *Nature Materials* **14**, 636-642 (2015).

9 Svensson, J., Anttu, N., Vainorius, N., Borg, B. M. & Wernersson, L.-E. Diameter-Dependent Photocurrent in InAsSb Nanowire Infrared Photodetectors. *Nano Letters* **13**, 1380–1385 (2013).

10 Thompson, M. D. *et al.* Low leakage-current InAsSb nanowire photodetectors on silicon. *Nano Letters* **16**, 182-187 (2015).

11 Rigutti, L. *et al.* Ultraviolet photodetector based on GaN/AlN quantum disks in a single nanowire. *Nano Letters* **10**, 2939-2943 (2010).

12 Karimi, M. *et al.* Room-temperature InP/InAsP Quantum Discs-in-Nanowire Infrared Photodetectors. *Nano Letters* **17**, 3356-3362, (2017).

13 Karimi, M. *et al.* Intersubband Quantum Disc-in-Nanowire Photodetectors with Normal-Incidence Response in the Long-Wavelength Infrared. *Nano Letters* **18**, 365-372, (2018).

14 Tatebayashi, J. *et al.* Room-temperature lasing in a single nanowire with quantum dots. *Nature Photonics* **9**, 501-505 (2015).

15 Erhard, N. *et al.* Ultrafast photodetection in the quantum wells of single AlGaAs/GaAs-based nanowires. *Nano Letters* **15**, 6869-6874 (2015).

16 Beaudoin, M. *et al.* Self-consistent determination of the band offsets in In As x P 1− x/InP strained-layer quantum wells and the bowing parameter of bulk In As x P 1− x. *Physical Review B* **53**, 1990 (1996).

17 Tinetti, G., Encrenaz, T. & Coustenis, A. Spectroscopy of planetary atmospheres in our Galaxy. *The Astronomy and Astrophysics Review* **21**, 63, (2013).

18 Rogalski, A. & Chrzanowski, K. Infrared devices and techniques. *Optoelectronics Review* **10**, 111-136 (2002).

19 Rogalski, A., Martyniuk, P. & Kopytko, M. Challenges of small-pixel infrared detectors: a review. *Reports on Progress in Physics* **79**, 046501 (2016).

20 Lawson, W., Nielsen, S., Putley, E. & Young, A. Preparation and properties of HgTe and mixed crystals of HgTe-CdTe. *Journal of Physics and Chemistry of Solids* **9**, 325-329 (1959).

21 Levine, B., Choi, K., Bethea, C., Walker, J. & Malik, R. New 10 μm infrared detector using intersubband absorption in resonant tunneling GaAlAs superlattices. *Applied Physics Letters* **50**, 1092-1094 (1987).

22 Phillips, J., Kamath, K. & Bhattacharya, P. Far-infrared photoconductivity in self-organized InAs quantum dots. *Applied physics letters* **72**, 2020-2022 (1998).

23 Capper, P. & Elliott, C. *Infrared detectors and emitters: materials and devices*. Vol. 8 (Springer Science & Business Media, 2013).

24 Rogalski, A. HgCdTe infrared detector material: history, status and outlook. *Reports on Progress in Physics* **68**, 2267 (2005).

25 Delaunay, P.-Y., Nguyen, B. M., Hofman, D. & Razeghi, M. Substrate removal for high quantum efficiency back side illuminated type-II In As⁄Ga Sb photodetectors. *Applied Physics Letters* **91**, 231106 (2007).

26 Haddadi, A., Dehzangi, A., Adhikary, S., Chevallier, R. & Razeghi, M. Background–limited long wavelength infrared InAs/InAs1− xSbx type-II superlattice-based photodetectors operating at 110 K. *APL Materials* **5**, 035502 (2017).

27 Haddadi, A., Chevallier, R., Dehzangi, A. & Razeghi, M. Extended short-wavelength infrared nBn photodetectors based on type-II InAs/AlSb/GaSb superlattices with an AlAsSb/GaSb superlattice barrier. *Applied Physics Letters* **110**, 101104 (2017).

28 Itsuno, A. M., Phillips, J. D. & Velicu, S. Mid-wave infrared HgCdTe nBn photodetector. *Applied Physics Letters* **100**, 161102 (2012).

29 Norton, P. HgCdTe infrared detectors. *Optoelectronics Review*, 159-174 (2002).

30 Soci, C. *et al.* Nanowire Photodetectors. *Journal of Nanoscience and Nanotechnology* **10**, 1430-1449, (2010).

31 Soci, C. *et al.* ZnO nanowire UV photodetectors with high internal gain. *Nano Letters* **7**, 1003-1009 (2007).

32 O'Brien, G. A., Quinn, A. J., Tanner, D. A. & Redmond, G. A single polymer nanowire photodetector. *Advanced Materials* **18**, 2379-2383 (2006).

33 Jelen, C., Slivken, S., Guzman, V., Razeghi, M. & Brown, G. J. InGaAlAs-InP quantum-well infrared photodetectors for 8-20-/spl mu/m wavelengths. *IEEE Journal of Quantum Electronics* **34**, 1873-1876 (1998).

34 Downs, C. & Vandervelde, T. E. Progress in infrared photodetectors since 2000. *Sensors* **13**, 5054-5098 (2013).

35 Guériaux, V. *et al.* Quantum well infrared photodetectors: present and future. *Optical Engineering* **50**, 061013 (2011).

36 Levine, B. Quantum-well infrared photodetectors. *Journal of Applied Physics* **74**, R1-R81 (1993).

37 Gunapala, S. & Bandara, S. in *Semiconductors and Semimetals* Vol. 62 197-282 (Elsevier, 1999).

38 Zhang, W. *et al.* High-detectivity InAs quantum-dot infrared photodetectors grown on InP by metal–organic chemical–vapor deposition. *Applied Physics Letters* **86**, 191103 (2005).

39 Kim, S. *et al.* Growth and characterization of InGaAs/InGaP quantum dots for midinfrared photoconductive detector. *Applied Physics Letters* **73**, 963-965 (1998).

40 Stiff-Roberts, A. D. Quantum-dot infrared photodetectors: a review. *Journal of Nanophotonics* **3**, 031607 (2009).

41 Rostami, A., Rasooli, H. & Baghban, H. *Terahertz technology: fundamentals and applications*. Vol. 77 (Springer Science & Business Media, 2010).

42 Weber, A. *et al.* Strong normal-incidence infrared absorption in self-organized InAs/InAlAs quantum dots grown on InP (001). *Applied Physics Letters* **74**, 413-415 (1999).

43 Tseng, C.-C. *et al.* Enhanced normal-incident absorption of quantum-dot infrared photodetectors with smaller quantum dots. *IEEE Photonics Technology Letters* **20**, 1240-1242 (2008).

44 Pan, D., Towe, E. & Kennerly, S. Strong normal-incidence infrared absorption and photo-current spectra from highly uniform (In, Ga) As/GaAs quantum dot structures. *Electronics Letters* **34**, 1019-1020 (1998).

45 Rogalski, A. Infrared detectors: status and trends. *Progress in Quantum Electronics* **27**, 59-210 (2003).

46 Sikorski, C. & Merkt, U. Spectroscopy of electronic states in InSb quantum dots. *Physical Review Letters* **62**, 2164 (1989).

47 Towe, E. & Pan, D. Semiconductor quantum-dot nanostructures: Their application in a new class of infrared photodetectors. *IEEE Journal of Selected Topics in Quantum Electronics* **6**, 408-421 (2000).

48 Krishna, S. *et al.* Two color InAs/InGaAs dots-in-a-well detector with background-limited performance at 91 K. *Applied Physics Letters* **82**, 2574-2576 (2003).

49 García de Arquer, F. P., Lasanta, T., Bernechea, M. & Konstantatos, G. Tailoring the electronic properties of colloidal quantum dots in metal–semiconductor nanocomposites for high performance photodetectors. *Small* **11**, 2636-2641 (2015).

50 Nguyen, B.-M. *et al.* Very high quantum efficiency in type-II In As⁄Ga Sb superlattice photodiode with cutoff of 12 μ m. *Applied Physics Letters* **90**, 231108 (2007).

51 Nguyen, B.-M., Bogdanov, S., Pour, S. A. & Razeghi, M. Minority electron unipolar photodetectors based on type II InAs/GaSb/AlSb superlattices for very long wavelength infrared detection. *Applied Physics Letters* **95**, 183502 (2009).

52 Hood, A., Razeghi, M., Aifer, E. H. & Brown, G. J. On the performance and surface passivation of type II InAs⁄GaSb superlattice photodiodes for the very-long-wavelength infrared. *Applied Physics Letters* **87**, 151113 (2005).

53 Smith, D. & Mailhiot, C. Proposal for strained type II superlattice infrared detectors. *Journal of Applied Physics* **62**, 2545-2548 (1987).

54 Li, J. V., Yang, R. Q., Hill, C. J. & Chuang, S. L. Interband cascade detectors with room temperature photovoltaic operation. *Applied Physics Letters* **86**, 101102 (2005).

55 Youngdale, E. *et al.* Auger lifetime enhancement in InAs–Ga1− x In x Sb superlattices. *Applied Physics Letters* **64**, 3160-3162 (1994).

56 LaPierre, R., Robson, M., Azizur-Rahman, K. & Kuyanov, P. A review of III–V nanowire infrared photodetectors and sensors. *Journal of Physics D: Applied Physics* **50**, 123001 (2017).

57 Wu, W., Bonakdar, A. & Mohseni, H. Plasmonic enhanced quantum well infrared photodetector with high detectivity. *Applied Physics Letters* **96**, 161107 (2010).

58 Liang, D. & Bowers, J. Photonic integration: Si or InP substrates? *Electronics Letters* **45**, 578-581 (2009).

59 Bi, Z. *et al.* InGaN Platelets: Synthesis and Applications toward Green and Red Light-Emitting Diodes. *Nano Letters* **19**, 2832-2839 (2019).

60 May, B. J. *et al.* Nanoscale electronic conditioning for improvement of nanowire light-emitting-diode efficiency. *ACS Nano* **12**, 3551-3556 (2018).

61 Xu, W.-Z. *et al.* Vertically emitting indium phosphide nanowire lasers. *Nano Letters* **18**, 3414-3420 (2018).

62 Eaton, S. W., Fu, A., Wong, A. B., Ning, C.-Z. & Yang, P. Semiconductor nanowire lasers. *Nature Reviews Materials* **1**, 16028 (2016).

63 Hill, D. J., Teitsworth, T. S., Ritchie, E. T., Atkin, J. M. & Cahoon, J. F. Interplay of Surface Recombination and Diode Geometry for the Performance of Axial p–i–n Nanowire Solar Cells. *ACS Nano* **12**, 10554-10563 (2018).

64 Memisevic, E. *et al.* Individual defects in InAs/InGaAsSb/GaSb nanowire tunnel field-effect transistors operating below 60 mV/decade. *Nano Letters* **17**, 4373-4380 (2017).

65 Cordoba, C. *et al.* Three-dimensional imaging of beam-induced biasing of InP/GaInP tunnel diodes. *Nano Letters* **19**, 3490-3497 (2019).

66 Calarco, R. *et al.* Nucleation and growth of GaN nanowires on Si (111) performed by molecular beam epitaxy. *Nano letters* **7**, 2248-2251 (2007).

67 Fuhrer, A. *et al.* Few electron double quantum dots in InAs/InP nanowire heterostructures. *Nano Letters* **7**, 243-246 (2007).

68 Van Tilburg, J. *et al.* Surface passivated InAs/InP core/shell nanowires. *Semiconductor Science and Technology* **25**, 024011 (2010).

69 Barrigón, E., Heurlin, M., Bi, Z., Monemar, B. & Samuelson, L. Synthesis and Applications of III–V Nanowires. *Chemical Reviews* **119**, 9170-9220 (2019).

70 Josefsson, M. *et al.* A quantum-dot heat engine operating close to the thermodynamic efficiency limits. *Nature Nanotechnology* **13**, 920 (2018).

71 Heurlin, M. *et al.* Continuous gas-phase synthesis of nanowires with tunable properties. *Nature* **492**, 90 (2012).

72 Wang, J., Gudiksen, M. S., Duan, X., Cui, Y. & Lieber, C. M. Highly polarized photoluminescence and photodetection from single indium phosphide nanowires. *Science* **293**, 1455-1457 (2001).

73 Tan, H. *et al.* Single-crystalline InGaAs nanowires for room-temperature high-performance near-infrared photodetectors. *Nano-Micro Letters* **8**, 29-35 (2016).

74 Ma, L. *et al.* Room-temperature near-infrared photodetectors based on single heterojunction nanowires. *Nano Letters* **14**, 694-698 (2014).

75 Shin, H. W. *et al.* Short-wavelength infrared photodetector on Si employing strain-induced growth of very tall InAs nanowire arrays. *Scientific Reports* **5**, 10764 (2015).

76 Kuyanov, P. & LaPierre, R. Photoluminescence and photocurrent from InP nanowires with InAsP quantum dots grown on Si by molecular beam epitaxy. *Nanotechnology* **26**, 315202 (2015).

77 Aiello, A., Hoque, A. H., Baten, M. Z. & Bhattacharya, P. High-Gain Silicon-Based InGaN/GaN Dot-in-Nanowire Array Photodetector. *ACS Photonics* **6**, 1289-1294 (2019).

78 Garcia, I., Galiana, B., Rey-Stolle, I. & Algora, C. MOVPE Technology for the Growth of III-V Semiconductor Structures. *Spanish Conference on Electron Devices.* (IEEE) 17-20, (2007)

79 Messing, M. E. *et al.* A comparative study of the effect of gold seed particle preparation method on nanowire growth. *Nano Research* **3**, 506-519 (2010).

80 Eriksson, T., Yamada, S., Krishnan, P. V., Ramasamy, S. & Heidari, B. High volume nanoimprint lithography on III/V substrates: Imprint fidelity and stamp lifetime. *Microelectronic Engineering* **88**, 293-299 (2011).

81 Hausmann, D., Becker, J., Wang, S. & Gordon, R. G. Rapid vapor deposition of highly conformal silica nanolaminates. *Science* **298**, 402-406 (2002).

82 Suyatin, D. B. *et al.* Strong Schottky barrier reduction at Au-catalyst/GaAs-nanowire interfaces by electric dipole formation and Fermi-level unpinning. *Nature Communications* **5**, 3221 (2014).

83 Yamada, T., Yamada, H., Lohn, A. J. & Kobayashi, N. P. Room-temperature Coulomb staircase in semiconducting InP nanowires modulated with light illumination. *Nanotechnology* **22**, 055201 (2010).

84 Wallentin, J., Ek, M., Wallenberg, L. R., Samuelson, L. & Borgström, M. T. Electron trapping in InP nanowire FETs with stacking faults. *Nano Letters* **12**, 151-155 (2011).

85 Ravikumar, A. P. *et al.* Room temperature and high responsivity short wavelength II-VI quantum well infrared photodetector. *Applied Physics Letters* **102**, 161107 (2013).

86 Chin, A., Liao, C., Chu, J. & Li, S. Investigation of Si-doped p-type AlGaAsGaAs, AlGaAsInGaAs quantum well infrared photodetectors and multiquantum wells grown on (3 1 1) A GaAs. *Journal of Crystal Growth* **175**, 999-1003 (1997).

87 Rota, M. B. *et al.* Bandgap energy of wurtzite InAs nanowires. *Nano Letters* **16**, 5197-5203 (2016).

88 Mishra, A. *et al.* Polarization and temperature dependence of photoluminescence from zincblende and wurtzite InP nanowires. *Applied Physics Letters* **91**, 263104 (2007).

89 Vurgaftman, I., Meyer, J. & Ram-Mohan, L. Band parameters for III–V compound semiconductors and their alloys. *Journal of Applied Physics* **89**, 5815-5875 (2001).

90 Mattila, M., Hakkarainen, T., Mulot, M. & Lipsanen, H. Crystal-structure-dependent photoluminescence from InP nanowires. *Nanotechnology* **17**, 1580 (2006).

91 Seyedi, M. A., Yao, M., O'Brien, J., Wang, S. & Dapkus, P. D. Large area, low capacitance, GaAs nanowire photodetector with a transparent Schottky collecting junction. *Applied Physics Letters* **103**, 251109 (2013).

92 Lee, W.-J. *et al.* High quantum efficiency nanopillar photodiodes overcoming the diffraction limit of light. *Nano Letters* **16**, 199-204 (2015).

93 Dan, Y., Zhao, X., Chen, K. & Mesli, A. A photoconductor intrinsically has no gain. *ACS Photonics* **5**, 4111-4116 (2018).

94 Ren, D. *et al.* Uncooled photodetector at short-wavelength infrared using InAs nanowire photoabsorbers on InP with p–n heterojunctions. *Nano Letters* **18**, 7901-7908 (2018).

95 Sharma, M. *et al.* Improved performance of GaAsSb/AlGaAs nanowire ensemble Schottky barrier based photodetector via in situ annealing. *Nanotechnology* **30**, 034005 (2018).

96 Svensson, J., Anttu, N., Vainorius, N., Borg, B. M. & Wernersson, L.-E. Diameter-dependent photocurrent in InAsSb nanowire infrared photodetectors. *Nano Letters* **13**, 1380-1385 (2013).

97 Karimi, M. *et al.* Room-temperature InP/InAsP quantum discs-in-nanowire infrared photodetectors. *Nano Letters* **17**, 3356-3362 (2017).

98 Li, D. *et al.* Ultra-fast photodetectors based on high-mobility indium gallium antimonide nanowires. *Nature Communications* **10**, 1664 (2019).

99 Zhou, Y. *et al.* Single crystalline SmB6 nanowires for self-powered, broadband photodetectors covering mid-infrared. *Applied Physics Letters* **112**, 162106 (2018).

100 Kischkat, J. *et al.* Mid-infrared optical properties of thin films of aluminum oxide, titanium dioxide, silicon dioxide, aluminum nitride, and silicon nitride. *Applied Optics* **51**, 6789-6798 (2012).

101 Seifert, W., Hessman, D., Liu, X. & Samuelson, L. Formation of interface layers in Ga x In1− x As/InP heterostructures: A re-evaluation using ultrathin quantum wells as a probe. *J Appl Phys* **75**, 1501-1510 (1994).

102 Camassel, J. *et al.* Finite interface effects for thin GaInAs/InP quantum wells grown by LP-MOVPE with a growth interruption sequence. *Journal of Crystal Growth* **107**, 543-548 (1991).

Infrared Photodetectors based on Nanowire Arrays with Embedded Quantum Heterostructures

Semiconductor nanowires have shown great potential for a broad range of electronics and optoelectronics applications such as transistors, lasers, LEDs and sensors due to their unique fundamental properties.

This thesis describes the development of a novel class of infrared photodetectors based on large arrays of InP NWs with embedded InAsP quantum heterostructures. The results might pave the way toward disruptive high-performance detection systems monolithically integrated with mainstream Si electronics.

Department of Physics
Faculty of Engineering
LUND UNIVERSITY

ISBN 978-91-7895-414-8

Printed by Media-Tryck, Lund 2019 NORDIC SWAN ECOLABEL 3041 0903